


Article

Preparation, Property Characterization of Gd₂YSbO₇/ZnBiNbO₅ Heterojunction Photocatalyst for Photocatalytic Degradation of Benzotriazole under Visible Light Irradiation

Ye Yao ¹  and Jingfei Luan ^{1,2,*} ¹ School of Physics, Changchun Normal University, Changchun 130032, China; yaoye1109@mails.jlu.edu.cn² State Key Laboratory of Pollution Control and Resource Reuse, School of the Environment, Nanjing University, Nanjing 210093, China

* Correspondence: jfluan@nju.edu.cn; Tel.: +86-(0)-199-5193-9498

Abstract: The Gd₂YSbO₇/ZnBiNbO₅ heterojunction photocatalyst was synthesized for the first time by the facile in situ precipitation method. The structural properties of a Gd₂YSbO₇/ZnBiNbO₅ heterojunction photocatalyst were characterized by X-ray diffractometer, scanning electron microscope-X ray energy dispersive spectra, X-ray photoelectron spectrograph and UV-Vis diffuse reflectance spectrophotometer. The band gap energy (BGE) of Gd₂YSbO₇ or ZnBiNbO₅ was found to be 2.396 eV or 2.696 eV, respectively. The photocatalytic property of Gd₂YSbO₇ or ZnBiNbO₅ or Gd₂YSbO₇/ZnBiNbO₅ heterojunction photocatalyst (GZHP) was reported. After a visible-light irradiation of 145 minutes (VLI-145 min), the removal rate (RER) of benzotriazole reached 99.05%, 82.45%, 78.23% or 47.30% with Gd₂YSbO₇/ZnBiNbO₅ heterojunction (GZH), Gd₂YSbO₇, ZnBiNbO₅ or N-doped TiO₂ (NTO) as photocatalyst. In addition, the kinetic constant k, derived from the dynamic curve toward benzotriazole concentration and visible light irradiation time with GZH as a photocatalyst, reached 0.0213 min⁻¹. Compared with Gd₂YSbO₇ or ZnBiNbO₅ or NTO, GZHP showed maximal photocatalytic activity (PHA) for the photocatalytic degradation of benzotriazole under visible-light irradiation. The RER of total organic carbon during the photocatalytic degradation of benzotriazole reached 90.18%, 74.35%, 70.73% or 42.15% with GZH as a photocatalyst or with Gd₂YSbO₇, ZnBiNbO₅ or NTO as a photocatalyst after VLI-145 min. Moreover, the kinetic constant k, which came from the dynamic curve toward total organic carbon concentration and visible light irradiation time with GZH as a photocatalyst, reached 0.0110 min⁻¹. Based on above results, GZHP showed the maximal mineralization percentage ratio when GZHP degraded benzotriazole. The results showed that hydroxyl radicals was the main oxidation radical during the degradation of benzotriazole. The photocatalytic degradation of benzotriazole with GZH as a photocatalyst conformed to the first-order reaction kinetics. Our research aimed to improve the photocatalytic properties of the single photocatalyst.

Keywords: Gd₂YSbO₇; Gd₂YSbO₇/ZnBiNbO₅ heterojunction photocatalyst; benzotriazole; photocatalytic degradation; visible-light irradiation; N-doped TiO₂; degradation pathway; degradation mechanism



Citation: Yao, Y.; Luan, J. Preparation, Property Characterization of Gd₂YSbO₇/ZnBiNbO₅ Heterojunction Photocatalyst for Photocatalytic Degradation of Benzotriazole under Visible Light Irradiation. *Catalysts* **2022**, *12*, 159. <https://doi.org/10.3390/catal12020159>

Academic Editors: Mohamed Ateia, Matthew Johnson and Božena Czech

Received: 31 December 2021

Accepted: 24 January 2022

Published: 27 January 2022

Publisher's Note: MDPI stays neutral with regard to jurisdictional claims in published maps and institutional affiliations.



Copyright: © 2022 by the authors. Licensee MDPI, Basel, Switzerland. This article is an open access article distributed under the terms and conditions of the Creative Commons Attribution (CC BY) license (<https://creativecommons.org/licenses/by/4.0/>).

1. Introduction

In recent years, environmental pollution issue has attracted more attention, especially sewage pollution problems, which are closely related to our daily life and health. Benzotriazole was one of most important synthetic compounds in plastic additives, which were used in large quantities in building materials and cooling and heating fluids, paints and dishwashing detergents, metal processing, aircraft deicing and anti-icing, and polymer stabilization [1,2]. Therefore, the environmental and health risk caused by benzotriazole had gradually attracted increasing attention all over the world. Furthermore, benzotriazole was highly water-solubility, and a great deal of residual benzotriazole had been measured in environmental samples [3–8]. Large amounts of residual pollutants in the water might

result in different degrees of benzotriazole bioaccumulation in an aquatic food web, and might finally be found in the human body. Due to its high water-solubility, low octanol water distribution coefficients, low vapor pressure and fair resistance to biodegradation [9–11] characters, the removal of benzotriazole had become more difficult.

Some traditional methods, such as electrochemistry [4–7], biodegradation [3,4,12], adsorption [8,9,13], and flocculation precipitation [9,11], had been utilized to remove the pollutant in wastewater, such as benzotriazole, alkylphenol, antioxidants, etc.; however, none of these methods had been good enough for use in a wide range of applications. Photocatalysis technology [14–16] was widely used in water-cleaning treatment and sewerage treatment due to its advantages of environmental protection, high treatment efficiency and low cost [17,18]. Photocatalyst technology could use sunlight as the energy to realize the activation of photocatalyst instead of using expensive oxidants, which made photocatalyst technology cheap, clean, attractive and promising from the perspective of energy [19]. Photocatalysts could purify sewage by decomposing organic pollutants to produce non-oxidation radicals. After use, the catalyst could be regenerated and recycled, which greatly reduced the cost of the photocatalyst.

The conventional photocatalysts were metal oxides such as TiO_2 and ZnO [20,21], considering the economic problems. However, due to its wide band gap, anatase TiO_2 could only absorb 5% of the solar energy, which corresponded to the ultraviolet light; thus, the rest of the optical energy was wasted. While exploring new photocatalysts, the abundant endeavors of previous scholars established the realization of the degradation of pollutants during visible light irradiation (VLIR) as a crucial goal for researchers. An important breakthrough was achieved as Zou reported that Ni-doped InTaO_4 compound had the ability to respond to the wavelength of visible-light regions in 2001. Zou proved that developing visible-light-responsive photocatalysts using the rest of the sunlight (43%) was possible. Latterly, photocatalysts with a formula of AB_2O_5 and $\text{A}_2\text{B}_2\text{O}_7$ were also reported. It was reported that Kapoor et al. [22] investigated the decomposition of gaseous acetaldehyde under UV light irradiation by MgTi_2O_5 with a pseudo-brookite structure type. Mixed metal oxide MgTi_2O_5 decomposed acetaldehyde under UV light irradiation. Zhang et al. [23] investigated the photocatalytic degradation (PHD) of methyl orange by $\text{La}_2\text{Ce}_2\text{O}_7$ powder. Ladan et al. [24] investigated the photocatalytic performance of the nanostructured $\text{Bi}_2\text{Sn}_2\text{O}_7$ in the degradation of the pollutant malachite green under solar light conditions.

Many effective methods had been used to improve the efficiency of the photocatalysts, such as the ion-doping method, heterojunction construction [25–30] and photosensitization [31,32]. Among them, the construction of composites was an active research field in the field of photocatalysis [29–35]. The function of a single photocatalyst could be improved by using the composite material system [36–40], which could possess a longer carrier life, higher photocatalytic performance and higher chemical stability [41–47]. In our previous work [48], we found that $\text{Sm}_2\text{FeSbO}_7$ had a pyrochlore type structure. As a photocatalyst under VLIR, its structural modification seemed to have the potential to improve the photocatalytic activity (PHA). Based on the above analysis, we could assume that substituting Sm^{3+} with Gd^{3+} , and substituting Fe^{3+} with Y^{3+} in $\text{Sm}_2\text{FeSbO}_7$, might increase the carrier concentration. The results showed that the electrical transmission and photophysical properties of the new Gd_2YSbO_7 (GYS) compound had been changed and improved, and the compound Gd_2YSbO_7 might have advanced photocatalytic properties.

In the photocatalysis process, the heterojunction catalyst showed excellent properties [49–51]. The heterojunction construction had a positive effect on the redox performance and electron transfer rate of the catalyst, which caused a high separative efficiency of photoinduced electron and photoinduced hole within two semiconductors [52]. Yu et al. [53] constructed the Bi/BiOCl heterojunction photocatalyst, which exhibited an extraordinarily high activity in the photodegradation of rhodamine B dye and persistent organic pollutants. Wang et al. [54] showed that the $\text{Ag}_2\text{O}/\text{Ag}_3\text{PO}_4$ heterostructure had a high degradation rate for methyl orange and phenol under VLIR in the photocatalytic test. The above results

showed that the construction of a photocatalyst with a heterojunction could significantly improve the redox performance of the photocatalyst [55] and improve the overall selectivity and activity of the reaction. In conclusion, the heterojunction construction of a catalyst was a promising application direction. Therefore, the $\text{Gd}_2\text{YSbO}_7/\text{ZnBiNbO}_5$ heterojunction photocatalyst (GZHP) was designed and synthesized.

In this paper, an X-ray diffraction (XRD), scanning electron microscope-X ray energy dispersive spectra (SEM-EDS), X-ray photoelectron spectrograph (XPS), and UV-Vis spectrophotometer were utilized to analyze the structural properties of pure phase Gd_2YSbO_7 and single-phase ZnBiNbO_5 prepared by the kinetic control method and high-temperature, solid-phase sintering method. In addition, the removal rate of benzotriazole under VLIR with Gd_2YSbO_7 as a photocatalyst, or ZnBiNbO_5 as a photocatalyst or N-doped TiO_2 (NTO) as a photocatalyst or $\text{Gd}_2\text{YSbO}_7/\text{ZnBiNbO}_5$ heterojunction (GZH) as a photocatalyst, was detected. The purpose of this study was to prepare a new heterojunction photocatalyst for removing benzotriazole from wastewater. The innovative research content of this paper was to synthesize a new type of Gd_2YSbO_7 nanocatalyst, using the high-temperature, solid-phase sintering method, for the first time. A visible light response photocatalyst with a high PHA was obtained, which could effectively remove benzotriazole. The removal of organic pollutants within dye wastewater with GZH as a photocatalyst was more efficient.

2. Result and Discussion

2.1. XRD Analysis

The structure of the as-prepared compound ZnBiNbO_5 is confirmed by XRD, as shown in Figure S1, with the JCPDS card of $\text{Y}_2\text{Ti}_2\text{O}_7$. The structure of the as-prepared product Gd_2YSbO_7 was also examined by XRD and Materials Studio program was used to obtain the collected data based on Rietveld analysis method. It could be concluded that Gd_2YSbO_7 or ZnBiNbO_5 was a single phase and the lattice parameter of the photocatalyst Gd_2YSbO_7 or ZnBiNbO_5 was 10.653(6) Å or 10.498(7) Å. At the same time, O atoms were considered in the refinement model; the good agreement between the observed and calculated intensities showed that Gd_2YSbO_7 or ZnBiNbO_5 crystalized in the cubic crystal with the space group Fd3m. Figure S2 shows the atomic structure of ZnBiNbO_5 . The atomic coordinates and structural parameters of Gd_2YSbO_7 and ZnBiNbO_5 are shown in Table S1 and Table S2, respectively.

It was known that the x coordinate of the O (1) atom could be considered as an index of the change in the crystal structure on the pyrochlore-type $\text{A}_2\text{B}_2\text{O}_7$ compounds (Cubic, space group Fd3m) and was equal to 0.375 when the six A-O (1) bond lengths were the same as that of the two A-O (2) bond lengths [56]. Therefore, information on the distortion of the MO_6 ($\text{M} = \text{Y}^{3+}$ and Sb^{5+}) octahedra could be gained from the x value [56]. The x value was shifted from $x = 0.375$ [56]; thus, the distortion of the MO_6 ($\text{M} = \text{Y}^{3+}$ and Sb^{5+}) octahedra clearly existed in the crystal structure of Gd_2YSbO_7 . Charge separation was required for the PHD of benzotriazole under VLIR for the sake of preventing recombination of the photoinduced electrons and photoinduced holes. Based on the reports of Inoue and Kudo, the local distortion of the MO_6 octahedra, obtained from some photocatalysts such as BaTi_4O_9 and $\text{Sr}_2\text{M}_2\text{O}_7$ ($\text{M} = \text{Nb}^{5+}$ and Ta^{5+}), was very important for preventing the charge recombination and contributed to the improvement in the PHA [57,58]. Therefore, the distortion of the MO_6 ($\text{M} = \text{Y}^{3+}$ and Sb^{5+}) octahedra in the crystal structure of Gd_2YSbO_7 could also be considered to be useful for enhancing the PHA. Gd_2YSbO_7 consisted of a three-dimensional network structure of corner-sharing MO_6 ($\text{M} = \text{Y}^{3+}$ and Sb^{5+}) octahedra. The MO_6 ($\text{M} = \text{Y}^{3+}$ and Sb^{5+}) octahedra were connected into chains by Gd^{3+} ion. Two kinds of Gd-O bond lengths coexisted: the six Gd-O (1) bond lengths (2.491 Å) were clearly longer than the two Gd-O (2) bond lengths (2.230 Å). The six M-O (1) ($\text{M} = \text{Y}^{3+}$ and Sb^{5+}) bond lengths was 2.020 Å, and the M-Gd ($\text{M} = \text{Y}^{3+}$ and Sb^{5+}) bond length was 3.642 Å. The M-O-M ($\text{M} = \text{Y}^{3+}$ and Sb^{5+}) bond angles were 128.640° in the crystal structure of Gd_2YSbO_7 . The Gd-M-Gd ($\text{M} = \text{Y}^{3+}$ and Sb^{5+}) bond angles were 135.00° in the crystal structure of Gd_2YSbO_7 . The Gd-M-O ($\text{M} = \text{Y}^{3+}$ and Sb^{5+}) bond angles were 139.203° in

the crystal structure of Gd₂YSbO₇. Based on the previous reports on the luminescent properties, when the M-O-M bond angle was closer to 180°, this helped the excited state become delocalized [56]. This showed that the angles between the corner-sharing MO₆ (M = Y³⁺ and Sb⁵⁺) octahedra, for example, the M-O-M bond angles for Gd₂YSbO₇, were important, affecting the PHA of Gd₂YSbO₇. The closer the M-O-M bond angles were to 180°, the larger the mobilities of the photoinduced electrons and photoinduced holes [56]. The mobilities of the photoinduced electrons and photoinduced holes affected the PHA because they affected the probability of electrons and holes reaching reaction sites on the catalyst surface [56].

In addition, the Gd–Y–O bond angle or Gd–Sb–O bond angle of Gd₂YSbO₇ was larger, which surely helped to increase the PHA of Gd₂YSbO₇. As in Gd₂YSbO₇, Gd was a 5d-block rare earth metal element, Y was a 4d-block metal element, and Sb was a 5p-block metal element. According to the above analysis, the effect of degrading benzotriazole under VLIR with Gd₂YSbO₇ as a photocatalyst could mainly be attributed to the crystalline structure and electronic structure.

2.2. UV-Vis Diffuse Reflectance Spectra

The absorption spectra of the Gd₂YSbO₇ sample and ZnBiNbO₅ sample are shown in Figure S3. The absorption edge of this new photocatalyst Gd₂YSbO₇ was found to be at 475 nm, which was at the visible region of the spectrum. The band gap energies of the crystalline semiconductors could be determined by the intersection point between photon energy $h\nu$ axis and the line extrapolated from the linear portion of the absorption edge of the so-called Kubelka–Munk Equation (1) (known as the re-emission equation) [59,60].

$$\frac{[1 - R_d(h\nu)]^2}{2R_d(h\nu)} = \frac{\alpha(h\nu)}{S} \quad (1)$$

where S was the scattering factor, and R_d was the diffuse reflectance, and α represented the absorption coefficient of radiation.

The optical absorption near the band edge of the crystalline semiconductors obeyed Equation (2) [61,62]:

$$\alpha h\nu = A (h\nu - E_g)^n \quad (2)$$

Here, A , α , E_g and ν represent proportional constant, absorption coefficient, band gap and light frequency, respectively. Within this equation, n controls the transition property of the semiconductor. Following the above equation, E_g and n could be determined: (1) plotting $\ln(\alpha h\nu)$ versus $\ln(h\nu - E_g)$ assuming an approximate value of E_g ; (2) deducing the value of n in accordance with the slope in this graph; (3) refining the value of E_g by plotting $(\alpha h\nu)^{1/n}$ versus $h\nu$ and extrapolating the plot to $(\alpha h\nu)^{1/n} = 0$. First, the direct method (1240/transition wavelength λ) was used to estimate the band gap E_g of Gd₂YSbO₇ or ZnBiNbO₅; as a result, the E_g of Gd₂YSbO₇ or ZnBiNbO₅ was estimated to be 2.226 eV (1240/557) or 2.562 eV (1240/484). Secondly, an indirect method (Equation (2)) was utilized to measure the precise band gap width of Gd₂YSbO₇ or ZnBiNbO₅ using 2.226 eV or 2.562 eV within Equation (2). Based on the above steps, the values of E_g for Gd₂YSbO₇ or ZnBiNbO₅ were calculated to be 2.396 eV or 2.696 eV. The value of n was about 0.5, which meant that the optical transition for Gd₂YSbO₇ was directly allowed. The value of n was about 2, which meant that the optical transition for ZnBiNbO₅ was indirectly allowed, as shown in Figure S3.

The band gap energy of Gd₂YSbO₇ or ZnBiNbO₅ was 2.396 eV or 2.696 eV, the band gap energy of Bi₃O₅I₂ was 2.02 eV [63], and the band gap energy of Co-doped ZnO was 2.39 eV [64]. The band-gap energies of all three compounds were less than 2.70 eV, which meant that the above four catalysts owned visible-light response characteristics and possess tremendous potential for displaying high catalytic activity under VLIR.

2.3. Property Characterization of $Gd_2YSbO_7/ZnBiNbO_5$ Heterojunction Photocatalyst

To obtain the surface chemical compositions and valence states of each element of GZHP, the X-ray photoelectron spectrum (XPS) was performed. Figure 1 presents the XPS survey spectrum of GZHP and Figure 2 shows the XPS spectra of O^{2-} , Gd^{3+} , Y^{3+} , Zn^{2+} , Bi^{3+} , Nb^{5+} and Sb^{5+} which derive from GZHP. Based on the full XPS spectrum, the synthesized GZHP included the elements of Gd, Y, Zn, Bi, Nb, Sb and O. According to the XPS analysis results, the oxidation state of Gd, Y, Zn, Bi, Nb, Sb or O ion was +3, +3, +2, +3, +5, +5 or -2 , respectively. Based on the above analysis results, that the chemical formula of the novel compound was Gd_2YSbO_7 and $ZnBiNbO_5$. In Figure 2, various elemental peaks with specific binding energies were obtained according to the peak-differentiating and -imitating (fitting procedure) results [65,66]. The O1s peak of the O element was located at 530.05 eV. The $Gd4d_{5/2}$ peak of the Gd element was located at 142.10 eV. The $Bi4f_{5/2}$ and $Bi4f_{7/2}$ peaks of Bi element were located at 164.20 eV and 159.07 eV. The $Sb3d_{3/2}$ peak or $Sb3d_{5/2}$ peak of the Sb element were located at 539.98 eV or 531.50 eV. The $Y3d_{3/2}$ and $Y3d_{5/2}$ peaks of the Y element were located at 158.55 eV and 157.02 eV. The $Nb3d_{3/2}$ and $Nb3d_{5/2}$ peaks of the Nb element were located at 209.40 eV and 206.60 eV. The $Zn2p_{1/2}$ peak of the Zn element were located at 1044.30 eV and the $Zn2p_{3/2}$ peak of the Zn element was located at 1021.65 eV. In brief, Figures 1 and 2 revealed the presence of gadolinium (Gd4d), yttrium (Y3p and Y3d), antimony (Sb3d and Sb4d), bismuth (Bi5d and Bi4f), zinc (Zn2p), niobium (Nb3d) and oxygen (O1s) within the prepared sample. The surface elemental analysis results displayed that the average atomic ratio of Gd:Y:Sb:Zn:Bi:Nb:O was 1146:592:579:586:612: 571:5914. The atomic ratio of Gd:Y:Sb or Zn:Bi:Nb in the sample of GZHP was 1.98:1.02:1.00 or 0.96:1.00:0.93, respectively. The atomic ratio of $Gd_2YSbO_7:ZnBiNbO_5$ was close to 581:590. The reason that the value of oxygen was high could be due to the amount of oxygen adsorbed on the surface of GZHP. Apparently, the XPS reflections did not show shoulders or widening, which was a strong proof that $Gd_2YSbO_7/ZnBiNbO_5$ was a pure phase without any other phases.

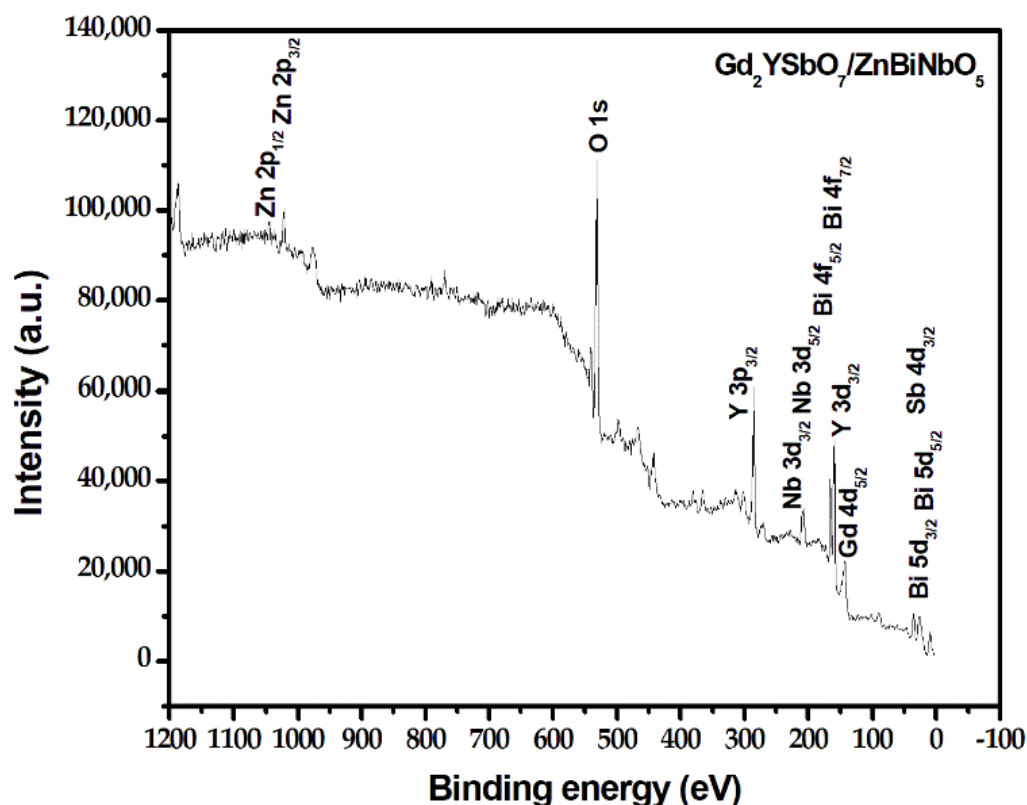


Figure 1. XPS survey spectrum of the GZHP.

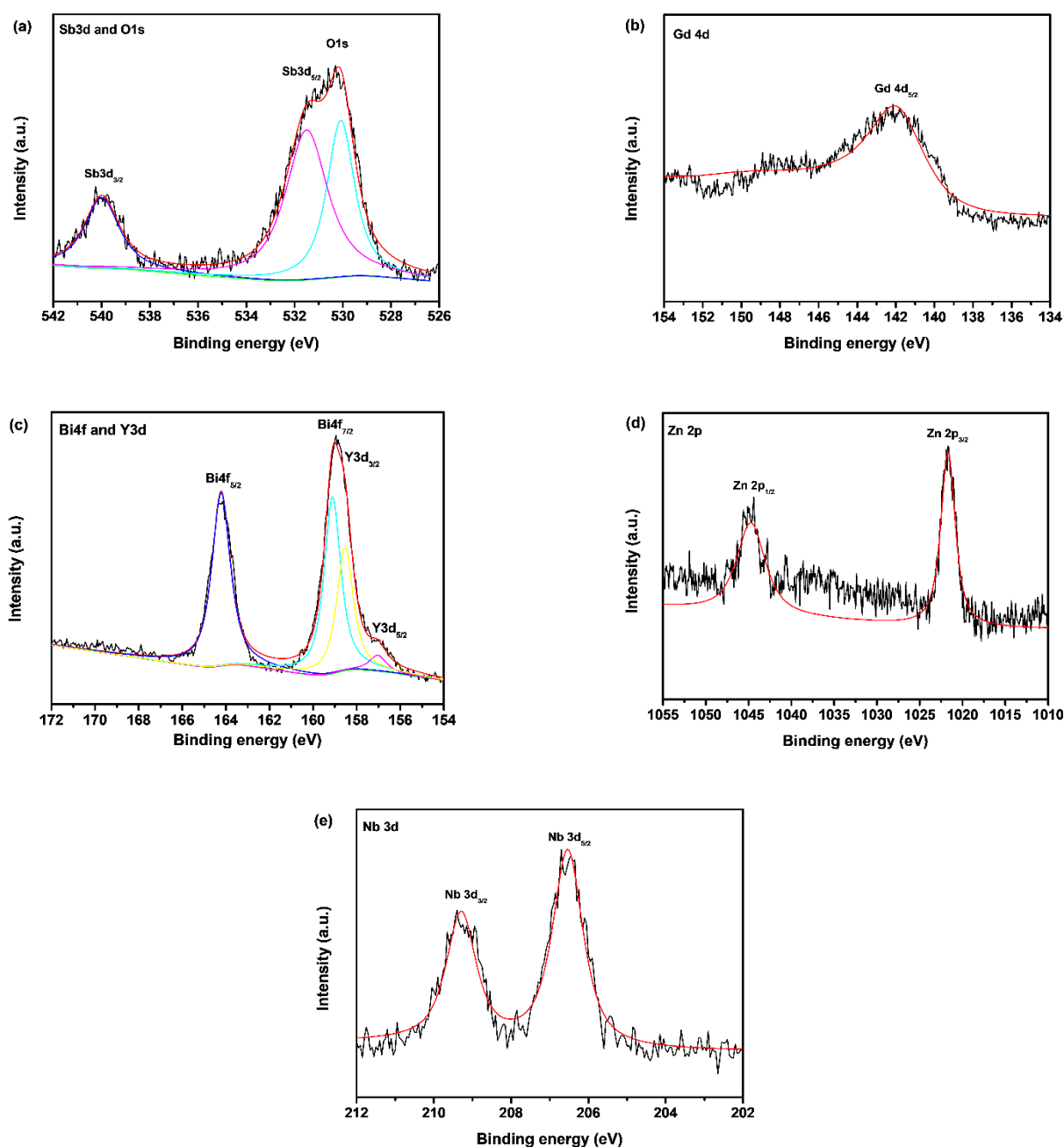


Figure 2. (a) XPS spectra of O^{2-} and Sb^{5+} derived from the GZHP; (b) XPS spectra of Gd^{3+} derived from the GZHP; (c) XPS spectra of Y^{3+} and Bi^{3+} derived from the GZHP; (d) XPS spectra of Zn^{2+} derived from the GZHP; (e) XPS spectra of Nb^{5+} derived from the GZHP.

Figures 3 and 4 show SEM images and the EDS elemental mapping of GZHP (Gd, Y, Sb, O from Gd_2YSbO_7 and Zn, Bi, Nb, O from $ZnBiNbO_5$). Figure 5 shows the EDS spectra of GZHP. Figures 3 and 4 show that the larger tetragonal particles belonged to Gd_2YSbO_7 and the smaller circular shaped particles belonged to $ZnBiNbO_5$. As could be seen from Figures 3 and 4, Gd_2YSbO_7 particles were surrounded by the smaller $ZnBiNbO_5$ particles, and these two particles were tightly combined, which indicated the successful synthesis of GZHP. Gd_2YSbO_7 possessed a rhombic-dodecahedron-like morphology. It was established that the structural growth in the photocatalyst was controlled by the different surface energies of the crystallite facets. Previously, researchers found the order of increasing surface energy for different facets of silver phosphate (111) < silver phosphate (100) < silver phosphate (110). Among them, the silver phosphate (110) facet showed a

higher surface energy than the (111) facet, which is the reason that irregularly shaped silver phosphate structures accumulate along the (110) crystallographic direction, leading to the formation of a rhombic-dodecahedron-like morphology for silver phosphate [67,68]. Therefore, the reason that Gd_2YSbO_7 has a rhombic-dodecahedron-like morphology could be explained by above explanation. The experimental results shown in Figure 3 indicated that ZnBiNbO_5 owned a regular, sphere, snowflake-like morphology and a homogeneous particle distribution. The particle size of ZnBiNbO_5 was measured to be around 750 nm, while the larger particle size of Gd_2YSbO_7 was measured to be about 2300 nm.

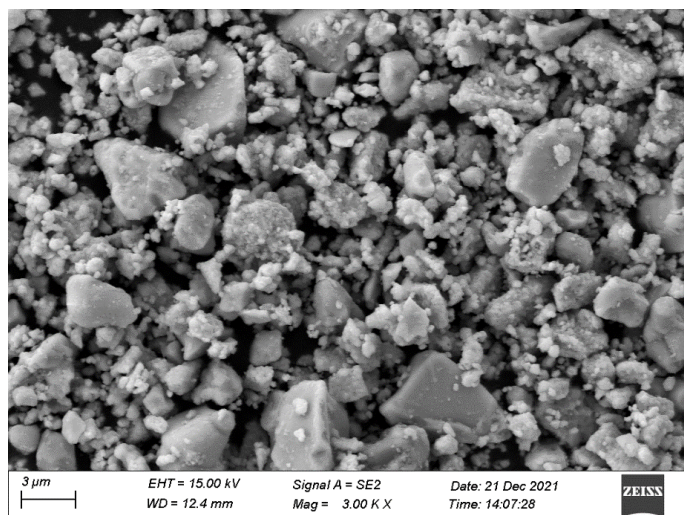


Figure 3. SEM photograph of $\text{Gd}_2\text{YSbO}_7/\text{ZnBiNbO}_5$ heterojunction photocatalyst.

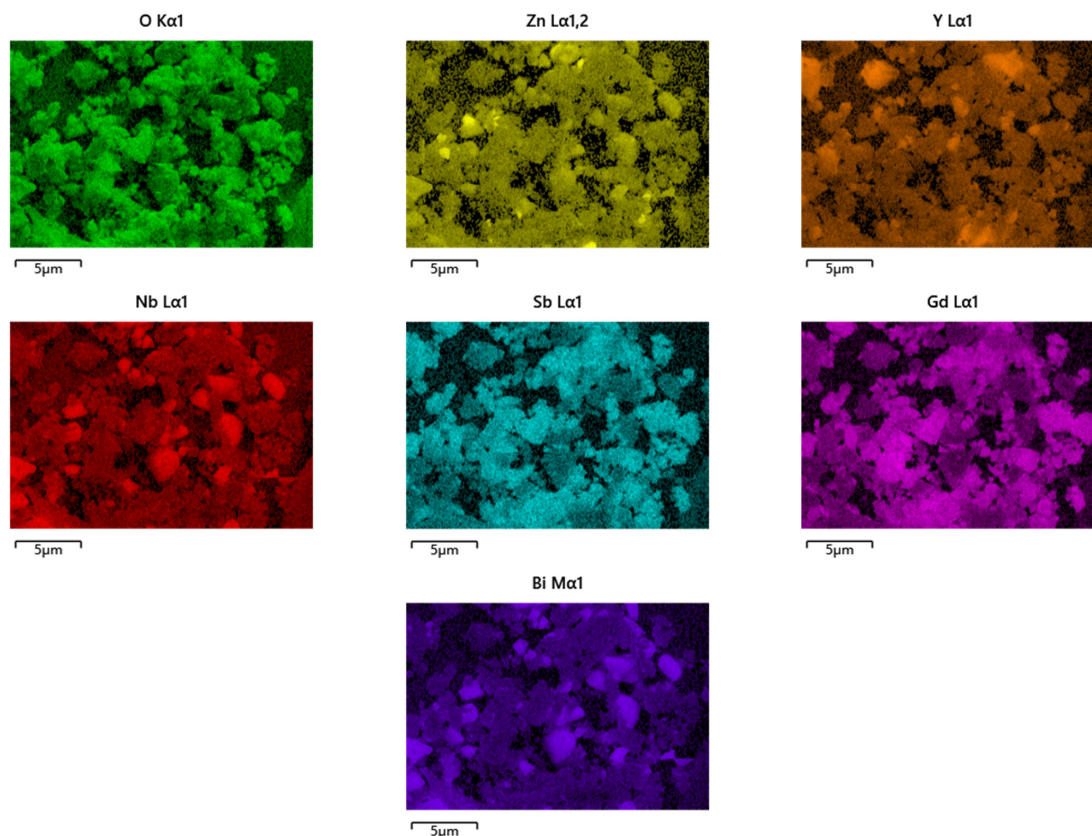


Figure 4. EDS elemental mapping of $\text{Gd}_2\text{YSbO}_7/\text{ZnBiNbO}_5$ heterojunction photocatalyst (Gd, Y, Sb, O from Gd_2YSbO_7 and Zn, Bi, Nb, O from ZnBiNbO_5).

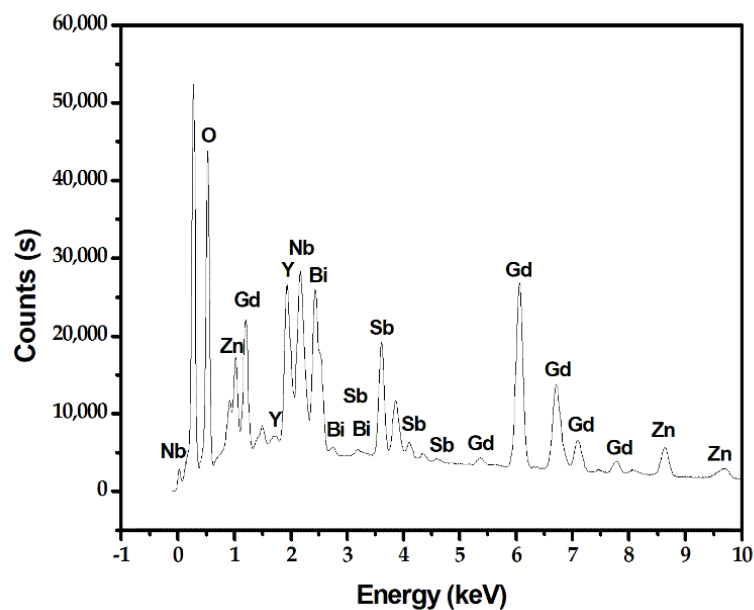


Figure 5. EDS spectrum of $Gd_2YSbO_7/ZnBiNbO_5$ heterojunction photocatalyst.

The SEM-EDS analysis results revealed that there were no other impure elements in the GZHP compound. At the same time, the pure phase of $ZnBiNbO_5$ was consistent with the X-ray diffraction analysis result displayed in Figure S1. It could be concluded from Figures 4 and 5 that the gadolinium element, yttrium element, antimony element, bismuth element, zinc element, niobium element and oxygen element are contained within GZHP. The above results are consistent with the XPS results of GZHP, shown in Figures 1 and 2. In accordance with the EDS spectrum of GZHP, the atomic ratio of Gd:Y:Sb:Zn:Bi:Nb:O was 1213:547:587:611:572:590:5880, which is also consistent with the XPS results of GZHP. The atomic ratio of $Gd_2YSbO_7:ZnBiNbO_5$ was close to 587:591. The more accurate stoichiometric ratio of the final product GZHP was summarized as 1168:1181 for $Gd_2YSbO_7:ZnBiNbO_5$. According to the above results, we could conclude that GZHP was of a high purity under our preparation conditions.

2.4. Photocatalytic Activity

Figure 6 presents the concentration variation (COV) curves of benzotriazole during PHD of benzotriazole with GZH as a photocatalyst, with Gd_2YSbO_7 as a photocatalyst, with $ZnBiNbO_5$ as a photocatalyst or with NTO as a photocatalyst under VLIR. Figure S4 shows the COV curves of benzotriazole during photocatalytic degradation of benzotriazole in the absence of photocatalyst under VLIR. Figure 6 shows that the removal rate (RER) of benzotriazole was 5.18%, 5.45%, 4.95% or 26.98% with GZH as a catalyst, Gd_2YSbO_7 as a catalyst, $ZnBiNbO_5$ as a catalyst or with NTO as catalyst under dark conditions for 45 min. Moreover, Figure S4 also shows that the RER of benzotriazole was 2.03% in the absence of a photocatalyst. Figure 6 shows that the concentration of benzotriazole within chemical industry wastewater gradually decreased with an increase in VLIR time. The results obtained from Figure 6 indicated that the removal rate of benzotriazole within chemical industry wastewater reached 99.05%, the reaction rate was $4.55 \times 10^{-9} \text{ mol}\cdot\text{L}^{-1}\cdot\text{s}^{-1}$ and the photonic efficiency was 0.0956% with GZH as a catalyst after visible light irradiation for 145 min (VLI-145 min). GZHP shows an outstanding removal efficiency in degrading benzotriazole compared with the normal photocatalysts, such as S-TiO₂, N-TiO₂, C-TiO₂ or CdS-TiO₂, after VLI-145 min, as shown in Table S3. All the other experiments followed the same VLI-145 min. When Gd_2YSbO_7 , which possessed the specific surface area of 4.12 m²/g and was prepared with the sintering temperature of 1320 °C for 50 h, was used as photocatalyst, the removal rate of benzotriazole reached 82.45%, the reaction rate was $3.79 \times 10^{-9} \text{ mol}\cdot\text{L}^{-1}\cdot\text{s}^{-1}$ and the photonic efficiency was 0.0796%. When the sintering

temperature was set as 950 °C for 50 h, the RER of benzotriazole reached 51.42% with mixed oxides as a catalyst after VLI-145 min. When the sintering temperature was set as 1450 °C for 50 h, the RER of benzotriazole reached 76.21% with Gd_2YSbO_7 , which owned the specific surface area of $3.07 \text{ m}^2/\text{g}$ as a catalyst after VLI-145 min. The removal rate of benzotriazole within chemical industry wastewater reached 78.23%, the reaction rate was $3.597 \times 10^{-9} \text{ mol}\cdot\text{L}^{-1}\cdot\text{s}^{-1}$ and the photonic efficiency was 0.0754% with ZnBiNbO_5 as a photocatalyst. The removal rate of benzotriazole reached 47.30%, the reaction rate was $2.17 \times 10^{-9} \text{ mol}\cdot\text{L}^{-1}\cdot\text{s}^{-1}$ and the photonic efficiency was 0.0456% with NTO as a photocatalyst. Moreover, the above results suggest that the photodegradation efficiency of benzotriazole in the presence of GZHP was the highest; meanwhile, the photodegradation efficiency of benzotriazole with Gd_2YSbO_7 as a photocatalyst was higher than that with ZnBiNbO_5 as a photocatalyst or with NTO as a photocatalyst. Ultimately, the photodegradation efficiency of benzotriazole with ZnBiNbO_5 as a photocatalyst was higher than that with NTO as a photocatalyst, indicating that the visible light PHA of GZHP was maximal compared with that of Gd_2YSbO_7 or ZnBiNbO_5 or NTO. The above results show that the removal rate of benzotriazole with GZH as a catalyst was 1.201 times or 1.266 times or 2.094 times higher than that with Gd_2YSbO_7 or ZnBiNbO_5 as photocatalysts, or with NTO as a photocatalyst, after VLI-145 min.

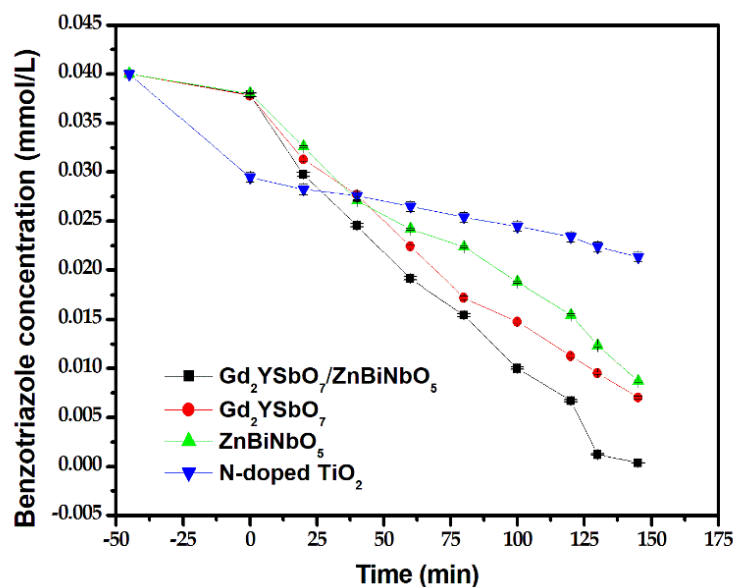


Figure 6. Concentration variation curves of benzotriazole during photocatalytic degradation of benzotriazole with GZH or Gd_2YSbO_7 as photocatalysts, or with ZnBiNbO_5 or NTO as photocatalysts under VLIR.

Figure 7 shows the COV curves of total organic carbon during the PHD of benzotriazole in chemical industry wastewater with GZH, Gd_2YSbO_7 , ZnBiNbO_5 or NTO as a photocatalyst under VLIR. The concentration of benzotriazole gradually decreased with an increase in VLIR time. As can be seen in Figure 7, the removal rate of total organic carbon within chemical industry wastewater reached 90.18%, 74.35%, 70.73% and 42.15%, respectively, after VLI-145 min when GZHP, Gd_2YSbO_7 , ZnBiNbO_5 and NTO were used to degrade benzotriazole. In conclusion, we can observe from the above results that the removal rate of total organic carbon during degrading benzotriazole in the presence of GZHP was higher than that in the presence of Gd_2YSbO_7 or ZnBiNbO_5 or NTO. The above results also indicate that the removal rate of total organic carbon during the degradation of benzotriazole in the presence of Gd_2YSbO_7 was much higher than that in the presence of ZnBiNbO_5 or NTO, which meant that GZHP showed the maximal mineralization percentage ratio when GZHP degraded benzotriazole compared with Gd_2YSbO_7 or ZnBiNbO_5 or NTO.

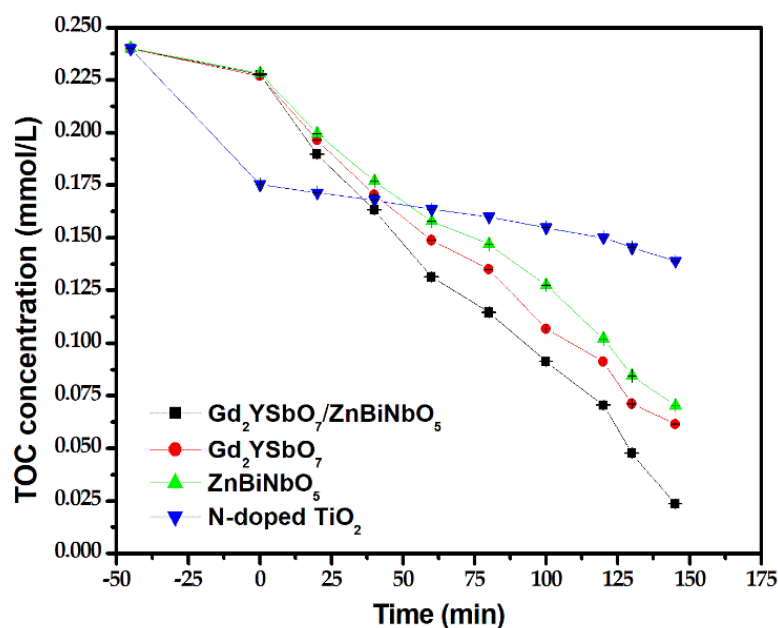


Figure 7. Concentration variation curves of total organic carbon during the photocatalytic degradation of benzotriazole in chemical industry wastewater with Gd₂YSbO₇/ZnBiNbO₅ heterojunction, Gd₂YSbO₇, ZnBiNbO₅ or NTO as a photocatalyst under VLIR.

Figure 8 presents the COV curves of benzotriazole during PHD with Gd₂YSbO₇/ZnBiNbO₅ heterojunction as a photocatalyst under VLIR for three cycle degradation tests. As seen in Figure 8, the removal rate of benzotriazole reached 97.25%, 96.08% or 94.90%, respectively, after VLI-145 min with GZH as a photocatalyst by accomplishing three cycle tests for degrading benzotriazole. Figure 9 shows the COV curves of total organic carbon during the PHD of benzotriazole with GZH as a catalyst under VLIR for three cycle degradation tests. From Figure 9, we can see that the removal rates of total organic carbon reach 88.19%, 87.02% or 85.27%, respectively. The experimental results obtained from Figures 8 and 9 show that the GZHP has a high stability.

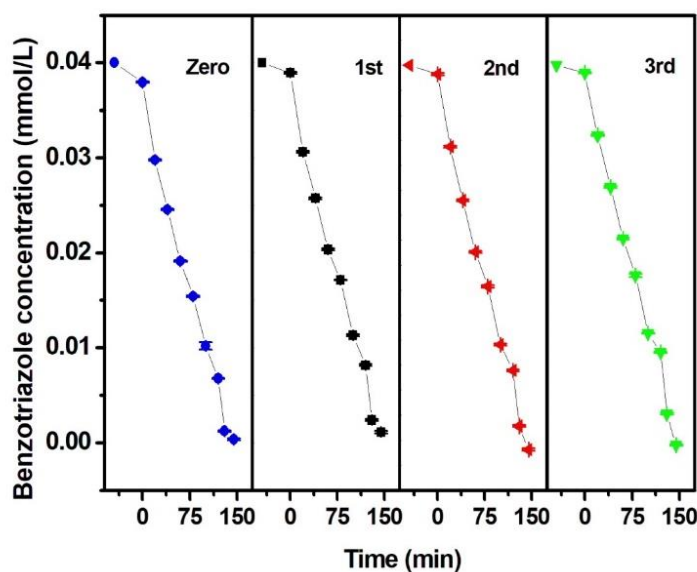


Figure 8. Concentration variation curves of benzotriazole during the photocatalytic degradation of benzotriazole in chemical industry wastewater with Gd₂YSbO₇/ZnBiNbO₅ heterojunction as photocatalyst under VLIR for three cycle degradation tests.

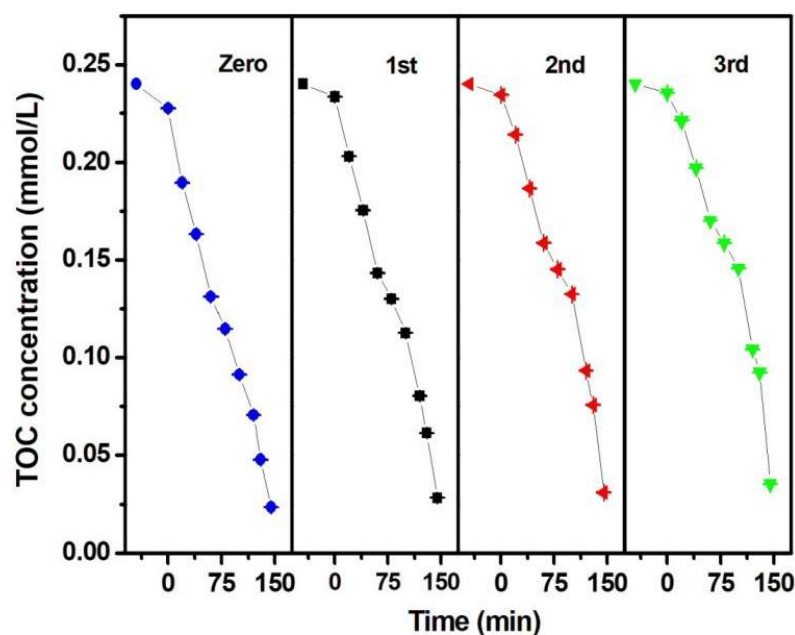


Figure 9. Concentration variation curves of total organic carbon during photocatalytic degradation of benzotriazole in chemical industry wastewater with $Gd_2YSbO_7/ZnBiNbO_5$ heterojunction as photocatalyst under VLIR for three cycle degradation tests.

Figure S5 shows the observed first-order kinetic plots for the PHD of benzotriazole with GZH, Gd_2YSbO_7 , $ZnBiNbO_5$ or NTO as a photocatalyst under VLIR. Based on Figure S5, the kinetic constant k , which was obtained from the dynamic curve toward benzotriazole concentration, and VLIR time with $Gd_2YSbO_7/ZnBiNbO_5$ heterojunction, Gd_2YSbO_7 , $ZnBiNbO_5$ or NTO as a photocatalyst reached 0.0213 min^{-1} , 0.0095 min^{-1} , 0.0077 min^{-1} or 0.0028 min^{-1} , respectively. The kinetic constant k , which came from the dynamic curve toward total organic carbon concentration, reached 0.0110 min^{-1} , 0.0075 min^{-1} , 0.0065 min^{-1} or 0.0023 min^{-1} with GZH, Gd_2YSbO_7 , $ZnBiNbO_5$ or NTO as a photocatalyst. The fact that the K_{TOC} value for degrading benzotriazole was lower than the value of K_C for degrading benzotriazole using the same catalyst illustrated that the intermediate photodegradation products of benzotriazole probably appeared during the PHD of benzotriazole under VLIR. Simultaneously, compared with the other three photocatalysts, GZHP presented a higher mineralization efficiency for benzotriazole degradation.

Figure S6 shows the observed first-order kinetic plots for the PHD of benzotriazole with $Gd_2YSbO_7/ZnBiNbO_5$ heterojunction as a photocatalyst under VLIR for three cycle degradation tests. Based on the results from Figure S6, the kinetic constant k , which was derived from the dynamic curve toward benzotriazole concentration and VLIR time with GZH as a catalyst for three cycle degradation tests, reached 0.0172 min^{-1} , 0.0152 min^{-1} or 0.0138 min^{-1} . The kinetic constant k , which came from the dynamic curve toward total organic carbon concentration and VLIR time with GZH as a catalyst for three cycle degradation tests, reached 0.0099 min^{-1} , 0.0089 min^{-1} or 0.0080 min^{-1} . According to the experimental results from Figures S5 and S6, the PHD of benzotriazole in chemical industry wastewater with GZH as a catalyst under VLIR conformed to the first-order reaction kinetics.

From Figure S6, the removal rate of benzotriazole is shown to decrease by 4.15% with GZH as a catalyst under VLIR after three cycle degradation tests, and the removal rate of total organic carbon decreased by 4.91%. No significant difference could be seen for the degradation efficiency in the above three cycle experiments, and the photocatalyst structure of GZHP was stable.

Figure 10 presents the effect of different radical scavengers, such as benzoquinone (BQ) or isopropanol (IPA) or ethylenediamine tetraacetic acid (EDTA), on the removal

rate of benzotriazole with GZH as a catalyst under VLIR. To determine the mechanism used to degrade benzotriazole, different radical scavengers were separately added to the benzotriazole solution at the beginning of the photocatalytic experiment. Isopropanol (IPA) was used to capture hydroxyl radicals ($\bullet\text{OH}$); Benzoquinone (BQ) was utilized to capture superoxide anions ($\bullet\text{O}_2^-$); Ethylenediaminetetraacetic acid (EDTA) was used to capture holes (h^+). The scheming IPA, BQ or EDTA concentration was 0.15 mmol L^{-1} , and the amount of IPA, BQ or EDTA added was 1 mL. According to Figure 10, while the IPA, BQ or EDTA were added to the benzotriazole solution, the removal rate of benzotriazole decreased by 68.16%, 59.41% or 36.75%, respectively, compared with the removal rate of benzotriazole that was derived from the control group. Thus, it could be concluded that $\bullet\text{OH}$, h^+ and $\bullet\text{O}_2^-$ were all active radicals during the benzotriazole degradation process. Figure 10 shows that $\bullet\text{OH}$ in the benzotriazole solution played a leading role when benzotriazole was degraded with GZH as a photocatalyst under VLIR. By adding a capture agent, the hydroxyl radicals was shown to possess a maximal oxidation removal ability for removing benzotriazole in chemical industry wastewater compared with superoxide anion or holes. The oxidation removal ability for degrading benzotriazole, which ranged from high to low among the three oxidation radicals, was as follows: hydroxyl radicals > superoxide anions > holes.

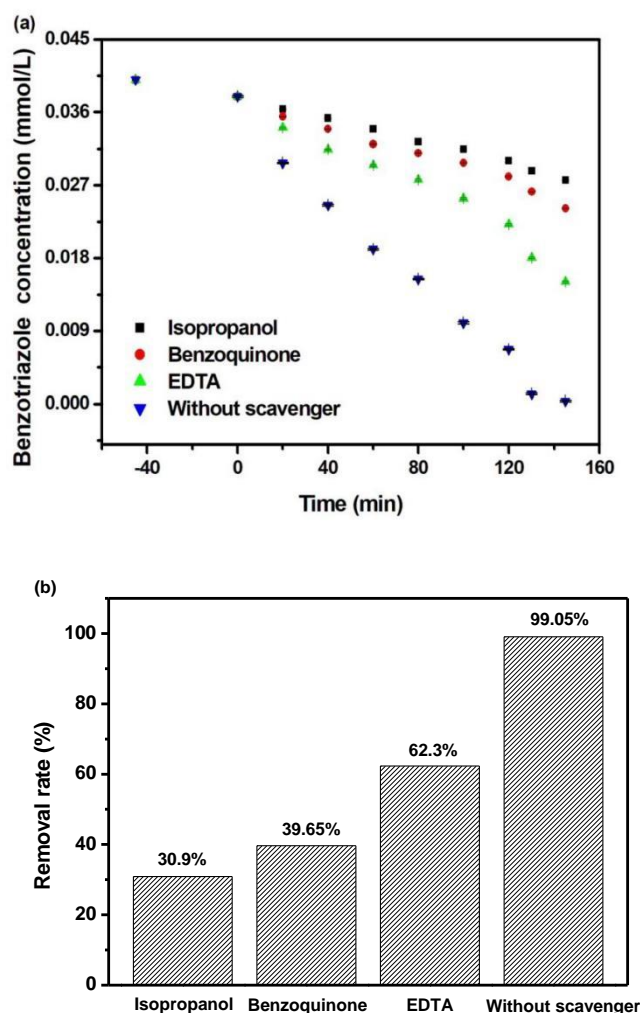


Figure 10. (a) Effect of different radical scavengers on the removal rate of benzotriazole with $\text{Gd}_2\text{YSbO}_7/\text{ZnBiNbO}_5$ heterojunction as photocatalyst under VLIR; (b) Effect of different radical scavengers such as benzoquinone (BQ), isopropanol (IPA) or ethylenediamine tetra-acetic acid (EDTA) on the removal efficiency of benzotriazole with $\text{Gd}_2\text{YSbO}_7/\text{ZnBiNbO}_5$ heterojunction as photocatalyst under VLIR.

Nyquist impedance plot measurement was another important characterization, which showed the photogenerated electron and photogenerated hole migration process of the prepared photocatalysts at solid/electrolyte interfaces. The smaller the arc radius, the higher the transportation efficiency of the photocatalysts. Figure S7 shows the corresponding Nyquist impedance plots of the prepared GZHP or Gd₂YSbO₇ photocatalyst or ZnBiNbO₅ photocatalyst. It could easily be seen that the diameter of the arc radius was in the order ZnBiNbO₅ > Gd₂YSbO₇ > GZHP. The above results indicate that the prepared GZHP presented a more efficient separation of the photogenerated electron and photogenerated hole, and a faster interfacial charge migration ability.

2.5. Possible Degradation Mechanism Analysis

Figure 11 shows the possible PHD mechanism of benzotriazole with GZH as a catalyst under VLIR. The potentials of the valence band (VB) and conductor band (CB) for the semiconductor catalyst could be calculated in accordance with Equation (3) and Equation (4), as follows [69]:

$$E_{CB} = X - E^e - 0.5E_g \quad (3)$$

$$E_{VB} = E_{CB} + E_g \quad (4)$$

where E_g presents the band gap of the semiconductor, X presents the electronegativity of the semiconductor, and E^e presents the energy of free electrons on the hydrogen scale, which was about 4.5 eV. According to the above equations, the VB potential or the CB potential for ZnBiNbO₅ were estimated to be 2.749 eV or 0.053 eV, respectively. For Gd₂YSbO₇, the VB potential or the CB potential were estimated to be 1.745 eV and −0.651 eV, respectively. Both ZnBiNbO₅ and Gd₂YSbO₇ could absorb visible light and internally generated electron–hole pairs when the GZHP was irradiated by visible light. Since the redox potential position of CB of Gd₂YSbO₇ (−0.651 eV) was more negative than that of ZnBiNbO₅ (0.053 eV), the electrons photoinduced on the CB of Gd₂YSbO₇ could transfer to the CB of ZnBiNbO₅. Additionally, the redox potential position of VB of ZnBiNbO₅ (2.749 eV) was more positive than that of Gd₂YSbO₇ (1.745 eV), and the photoinduced holes on the VB of ZnBiNbO₅ could transfer to the VB of Gd₂YSbO₇. Therefore, the coupling of ZnBiNbO₅ and Gd₂YSbO₇ to produce GZHP could effectively reduce the recombination rate of photoinduced electrons and photoinduced holes, and subsequently decrease the internal resistance, and prolong the lifetime of photo-induced electrons and photo-induced holes, as well as enhancing the interfacial charge transfer efficiency [70]. As a result, more oxidative radicals, such as •OH or •O₂[−], could be produced to improve the degradation efficiency of benzotriazole. Moreover, the CB potential of Gd₂YSbO₇ was −0.651 eV, which is more negative than that of O₂/•O₂[−] (−0.33 V), indicating that the electrons within the CB of Gd₂YSbO₇ could absorb oxygen to produce •O₂[−], which could degrade benzotriazole (as shown as path 1 in Figure 11). At the same time, the VB potential of ZnBiNbO₅ was 2.749 eV, which was more positive than that of OH[−]/•OH (2.38 V), indicating that the holes in the VB of ZnBiNbO₅ could oxidize H₂O or OH[−] into •OH to degrade benzotriazole, as shown as path 2. As shown in path 3, the benzotriazole could be oxidized and degraded directly because of the strong oxidizing ability of the holes that were photoinduced in the VB of Gd₂YSbO₇ or ZnBiNbO₅. In sum, the excellent PHA of GZHP toward benzotriazole degradation was mainly credited to the high efficiency of the electron–hole separation induced by GZHP.

To study the degradation mechanism of benzotriazole, the intermediate products that were generated during the degradation process of benzotriazole were detected by LC–MS. The intermediate products obtained during the PHD of benzotriazole were identified as C₆H₅N₃O ($m/z = 136$), C₇H₇N₃ ($m/z = 134$), C₅H₅N₃O₂ ($m/z = 138$), C₅H₅N₃O₄ ($m/z = 172$), C₆H₅N₃O₄ ($m/z = 184$), C₄H₃N₃O₄ ($m/z = 158$), C₆H₅N₃O₂ ($m/z = 152$), C₄H₅N₃O₂ ($m/z = 128$) and C₇H₇N₃O ($m/z = 150$). According to the above-detected intermediate products, the PHD pathway of benzotriazole was proposed. Figure 12 presents the suggested PHD pathway scheme of benzotriazole under VLIR with Gd₂YSbO₇/ZnBiNbO₅ heterojunction as a photocatalyst. Figure 12 shows that the oxidation reaction and methylation reaction of the triazole ring were

realized during the PHD process of benzotriazole. As expected, benzotriazole was converted into small-molecule organic compounds; therefore, the new small-molecule products could combine with other organic active groups and finally turn into CO₂ and water.

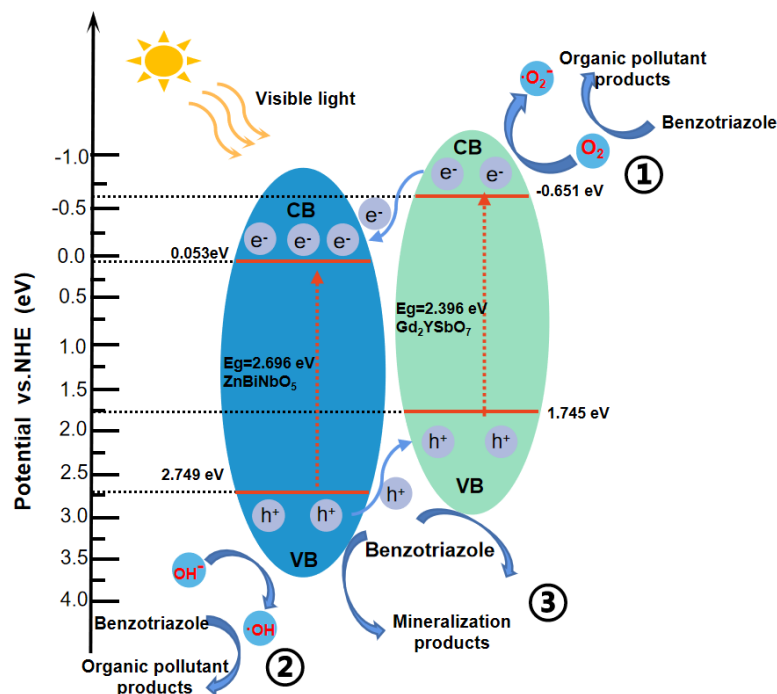


Figure 11. Possible photocatalytic degradation mechanism of benzotriazole with Gd₂Ysbo₇/ZnBibno₅ heterojunction as photocatalyst under VLIR.

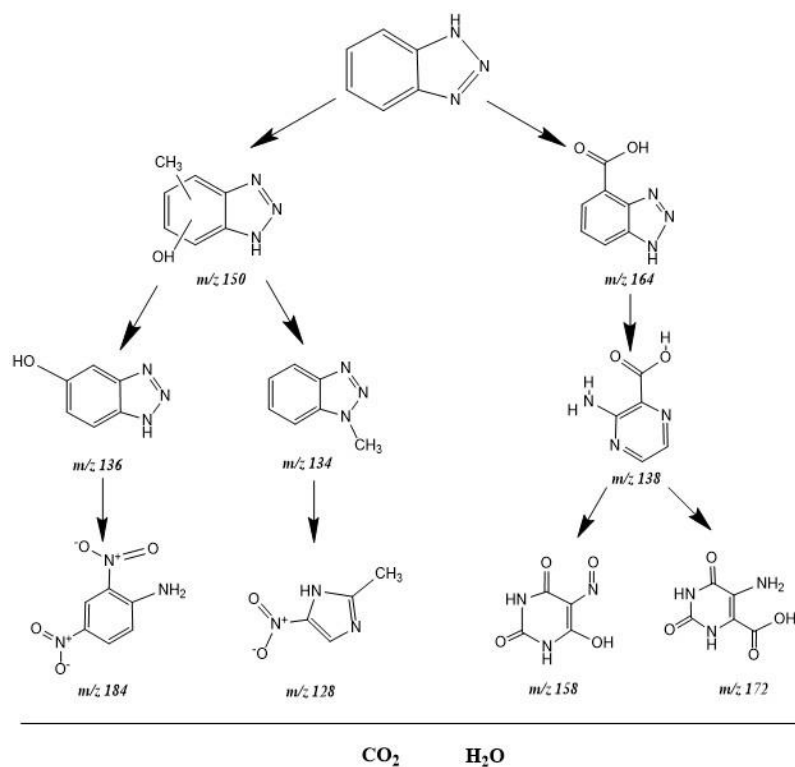


Figure 12. Suggested photocatalytic degradation pathway scheme for benzotriazole under VLIR with Gd₂Ysbo₇/ZnBibno₅ heterojunction as photocatalyst.

3. Experimental Section

3.1. Materials and Reagents

Ethylenediaminetetraacetic acid (EDTA, C₁₀H₁₆N₂O₈, purity = 99.5%) and isopropyl alcohol (IPA, C₃H₈O, purity ≥ 99.7%) were analytical grade. P-benzoquinone (BQ, C₆H₄O₂, purity ≥ 98.0%) was chemical grade. Moreover, the above chemical reagents were all purchased from Sinopharm Group Chemical Reagent Co., Ltd. (Beijing, China). Absolute ethanol (C₂H₅OH, purity ≥ 99.5%) conformed to American Chemical Society Specifications and was purchased from Aladdin Group Chemical Reagent Co., Ltd. (Beijing, China). Benzotriazole (C₆H₅N₃, purity ≥ 98%) was gas chromatography grade and was purchased from Tianjin Bodi Chemical Co., Ltd., Tianjin, China as the model material. Ultra-pure water (18.25 MU cm) was utilized throughout this work.

3.2. Preparation Method of Gd₂YSbO₇

Gd₂YSbO₇ was synthesized by solid-phase sintering method at a high temperature using Gd₂O₃ (99.99%), Y₂O₃ (99.99%) and Sb₂O₅ (99.99%) (Sinopharm Group Chemical Reagent Co., Ltd, Shanghai, China). In order to confirm the molar ratio of the raw oxides, the volatility of the raw oxide was tested using the following procedures: 1 g Gd₂O₃, 1 g Y₂O₃ and 1 g Sb₂O₅ were separately weighed and ground for 3 h in an agate mortar, and the above three raw oxides were separately placed in the alumina crucible (Shenyang Crucible Co., LTD, Shenyang, China) and then calcined at 1320 °C for 20 h in a high-temperature electric furnace (KSL 1700X, Hefei Kejing Materials Technology CO., LTD, Hefei, China). After cooling to room temperature, the three raw oxides were weighed again. As Gd₂O₃, Y₂O₃ or Sb₂O₅ still weighed 1 g after high-temperature sintering, the above three raw oxides were not volatile at 1320 °C. Therefore, a final molar ratio of n(Gd₂O₃):n(Y₂O₃):n(Sb₂O₅) = 2:1:1 was determined. Before the experiment, all powders were dried at 200 °C for 4 h. The precursors were stoichiometrically (n(Gd₂O₃):n(Y₂O₃):n(Sb₂O₅) = 2:1:1) mixed, then pressed into small columns, placed into an alumina crucible and calcined at 400 °C for 2 h. When naturally cooled to room temperature, the raw materials and the small columns were taken out of the electric furnace. The mixed materials should be ground and, subsequently, these mixed materials should be put into the electric furnace. Ultimately, the calcination process was separately carried out at 1320 °C for 50 h in an electric furnace. To clarify the preparation technology, a schematic representation of the synthesis process of the Gd₂YSbO₇ is shown in Figure S8a.

3.3. Preparation Method of ZnBiNbO₅

ZnBiNbO₅ was synthesized by the solid-phase sintering method at a high temperature using ZnO (99.99%), Bi₂O₃ (99.99%) and Nb₂O₅ (99.99%) (Sinopharm Group Chemical Reagent Co., Ltd., Shanghai, China). In order to confirm the molar ratio of the raw oxides, the volatility of the raw oxides was tested using the following procedures: 0.02 mol ZnO, 0.01 mol Bi₂O₃ and 0.01 mol Nb₂O₅ were separately weighed and were ground for 3 h in an agate mortar; the above three oxides were separately placed in an alumina crucible (Shenyang Crucible Co., LTD, Shenyang, China) and then calcined at 1100 °C for 25 h in a high-temperature electric furnace (KSL 1700X, Hefei Kejing Materials Technology CO., LTD, Hefei, China). After naturally cooling to room temperature, the quality of ZnO or Bi₂O₃ or Nb₂O₅ was remeasured and converted to a mole mass again. The results showed that 0.02 mol ZnO and 0.01 mol Nb₂O₅ remained unchanged. However, only 0.008 mol Bi₂O₃ was left, which meant that, when the temperature was 1100 °C, the Bi₂O₃ would be volatile. After five failed experiments, we concluded that the mole mass of 20% for Bi₂O₃ volatilized; as a result, the actual mole mass dosage of Bi₂O₃ should be 120% of the planned dosage. Therefore, a final molar ratio of n(ZnO):n(Bi₂O₃):n(Nb₂O₅) = 2:1.2:1 was determined.

These fully mixed materials were stoichiometrically (n(ZnO):n(Bi₂O₃):n(Nb₂O₅) = 2:1.2:1) quantified and put into a ball mill to obtain the final partial size of 1–2 μm. To ensure purity, all the powders were dried at 200 °C for 4 h before synthesis. Then, these powders were mixed in an aluminum oxide crucible after pressing into disks and, finally, these powders were sintered

in an electric furnace at 400 °C for 8 h. After crushing and pressing, the mixture was sintered again in an electric furnace at 1100 °C for 25 h. Finally, pure ZnBiNbO₅ catalyst was obtained after total grinding. To clarify the above preparation technology, a schematic representation of the synthesis process of the ZnBiNbO₅ is shown in Figure S8b.

3.4. Synthesis of N-Doped TiO₂

Nitrogen-doped titania (NTO) catalyst was prepared by sol-gel method; as a result, the precursor and solvent were tetrabutyl titanate and ethanol, respectively. Then, the following steps were carried out: (1) Solution A was made with 17 mL tetrabutyl titanate and 40 mL absolute ethyl alcohol; (2) Solution B consisted of 40 mL absolute ethyl alcohol, 10 mL glacial acetic acid and 5 mL double distilled water; (3) Under magnetic stirring condition, solution A was added drop by drop into solution until a transparent colloidal suspension was formed; (4) Aqua ammonia (N/Ti proportion was 8 mol%) was put into colloidal suspension and the magnetic stirring condition was maintained for 1 h. Next, the xerogel was generated after being aged for 2 days. The xerogel was ground into powder, which was calcined at 500 °C for 2 h; subsequently, the above powder was ground in agate mortar and screened by shaker to obtain NTO powders.

3.5. Synthesis of Gd₂YSbO₇/ZnBiNbO₅ Heterojunction Photocatalyst

First, 0.30 mol/L Gd(NO₃)₃·6H₂O, 0.15 mol/L Y(NO₃)₃·6H₂O and 0.15 mol/L SbCl₅ were mixed and stirred for 20 h. The aforementioned solution was transferred into a Teflon-lined autoclave, and then the temperature was raised to 200 °C for 15 h. Subsequently, the obtained powder was calcined at 800 °C for 10 h in a tube furnace at a rate of 8 °C/min under an atmosphere of N₂. Gd₂YSbO₇ powder was finally obtained. Secondly, 0.30 mol/L Zn(NO₃)₂·6H₂O, 0.15 mol/L Bi(NO₃)₃·5H₂O and 0.15 mol/L NbCl₅ were mixed and stirred for 20 h. This solution was transferred into a Teflon-lined autoclave and heated at 200 °C for 15 h. Subsequently, the obtained powder was calcined at 790 °C for 10 h in a tube furnace at a rate of 8 °C/min under an atmosphere of N₂. ZnBiNbO₅ powder was finally obtained.

A facile solvothermal method [71] was utilized to synthesize the new GZHP in this paper. GZHP was prepared by mixing 400 mg of Gd₂YSbO₇ with 400 mg of ZnBiNbO₅ in 200 mL of octanol (C₈H₁₈O); then, the ultrasonic bath was used to disperse for 1 h. The mixture was then heated and refluxed at 140 °C for 2 h under vigorous stirring conditions to improve attachment of ZnBiNbO₅ to the surface of Gd₂YSbO₇ nanoparticles to form GZHP. After being cooled to room temperature, the products were collected by centrifugation and then the mixture of n-hexane/ethanol was utilized to wash the sample several times. At last, the purified powders were dried at 60 °C for 6 h. Finally, GZHP was successfully prepared. To clarify this preparation technology, a schematic representation of the synthesis process of the Gd₂YSbO₇/ZnBiNbO₅ heterojunction photocatalyst is shown in Figure S8c.

3.6. Characterizations

The pure crystals of the prepared samples were examined by the powder X-ray diffractometer (XRD, Shimadzu, XRD-6000, Cu K α radiation, $\lambda = 1.5418 \text{ \AA}$, sampling step length of 0.02°, preset time of 0.3 s step⁻¹, 2 theta of 10–80°). The scanning speed of the XRD instrument was 70°, which took 70 min; thus, each degree took 60 s. Each degree was divided into 50 steps, and each step took 1.2 s. The morphology and microstructure of the prepared samples were characterized using scanning electron microscope (SEM, FEI, Quanta 250) and the elementary composition derived from the samples prepared above prepared was captured by energy-dispersive spectroscopy (EDS). SEM minimized the amount of sample preparation required, and the low vacuum and ESEM abilities enabled charge-free imaging and analysis. Quanta's patented "through-the-lens" differential pressure vacuum technology enabled EDS and EBSD analysis of samples under high- and low-vacuum conditions for enhanced analytical abilities. Stable high beam current (up to 2 μA) enabled fast and accurate analysis. The surface of the sample was plated with gold, and the catalyst powder

was evenly coated on the disk to complete the surface imaging and obtain surface morphology and composition information for the sample. A diffuse reflectance spectrum was obtained for the sample prepared above using an UV-Vis spectrophotometer (UV-Vis DRS, Shimadzu, UV-3600). Shimadzu UV-3600 could extend the measurement range from the most common single-beam spectrophotometer to a deep UV-VIS-NIR spectrophotometer for UV and NIR regions. Photomultiplier tubes were used in the ultraviolet and visible regions; InGaAs and PbS detectors were used in the near-infrared region. The InGaAs detector covered the weak range of photomultiplier tubes and PbS detectors, ensuring high sensitivity over the entire measurement range. The surface chemical composition and states of the prepared sample were analyzed by X-ray photoelectron spectrograph (XPS, UIVAC-PHI, PHI 5000 VersaProbe) with an Al- $K\alpha$ X-ray source. The PHI 5000 VersaProbe was a multifunctional analytical instrument for PHI Scanning XPS Microprobe Devices in PHI's industry-leading ZL Scanning X-Ray Technology and ZL Dual Beam Neutralization Technology. Scanning focused X-ray technology was the core technology of VersaProbe. Monochromatic, scanning, and focused X-ray sources allowed for a better analysis of microscopic and macroscopic regions, and all X-ray settings (including those with a beam spot diameter of less than 10 μm) could be used for spectral analysis, depth profiling and image analysis.

3.7. Photoelectrochemical Experiments

The electrochemical impedance spectroscopy (EIS) experiment was performed by a CHI660D electrochemical station (Chenhua Instruments Co. Shanghai, China) with a standard three-electrode. The three-electrode consisted of a working electrode (as-prepared catalysts), counter-electrode (platinum plate) and reference electrode (Ag/AgCl electrode). The electrolyte was Na_2SO_4 aqueous solution (0.5 mol/L). The light source for the experiment was a 500 W Xe lamp with a UV cut-off filter. The preparation of the working electrode was as follows: we placed the sample (0.03 g) and chitosan (0.01 g) in dimethylformamide (0.45 mL), and then we used ultrasonic treatment for an hour to obtain a uniform suspension solution. Subsequently, they were trickled on indium tin oxide (ITO)-conducting glass (10 mm \times 20 mm). At last, the working electrode was dried at 80 $^\circ\text{C}$ for 10 min.

3.8. Experimental Setup and Procedure

All the experiments were carried out in a photocatalytic reactor (XPA-7, Xujiang Electromechanical Plant, Nanjing, China) and the temperature of the reaction system was 20 $^\circ\text{C}$, controlled by circulating cooling water. Simulated sunlight irradiation was provided by a 500 W xenon with a 420 nm cut-off filter. For the same 12 quartz tubes, the volume of a single reaction solution was 40 mL, and the total reaction volume for chemical industry wastewater was 480 mL. The dosage of Gd_2YSbO_7 or ZnBiNbO_5 or GZHP was 0.75 g/L; the concentration of benzotriazole was 0.040 mmol/L. The concentration of benzotriazole was the residual concentration after biodegradation for practical chemical industry wastewater, which contained a benzotriazole concentration of 1.2 mmol/L. During the reaction, 3 mL suspension was periodically withdrawn, and 27 mL suspension was taken to measure the concentration of residual benzotriazole after VLI-145 min; subsequently, the filtration (0.22 μm PES polyether sulfone filter membrane) was used to remove the catalyst. Finally, the residual concentration of benzotriazole in solution was determined by Agilent 200 high-performance liquid chromatography (Agilent Technologies, Palo Alto, CA, USA) with an UV detector and a Zorbax 300SB-C18 column (4.6 mm \times 150 mm, 5 μm). The mobile phase consisted of 50% CH_3CN and 50% distilled deionized water. The UV detection wavelengths were located at 254 nm. The injection volume of post-photodegradation benzotriazole solution was 10 μL , and the flow rate was 1 $\text{mL}\cdot\text{min}^{-1}$. Prior to VLIR, we maintained magnetic stirring conditions in darkness for 45 min to guarantee the suspension (contained the photocatalyst and benzotriazole) in adsorption/desorption equilibrium among the photocatalyst, benzotriazole and atmospheric oxygen. During VLIR, the suspension was stirred at 500 rpm.

The mineralization experimental data for benzotriazole within the reaction solution were measured using a total organic carbon analyzer (TOC-5000 A, Shimadzu Corporation, Kyoto, Japan). To detect the concentration of total organic carbon during the PHD of benzotriazole, potassium acid phthalate ($\text{KHC}_8\text{H}_4\text{O}_4$) or an anhydrous sodium carbonate was utilized as a standard reagent. Standard solutions of potassium acid phthalate with a known carbon concentration (in the range of 0–100 mg/L) were prepared for calibration purposes. Nine samples, which contained 68 mL reaction solution, were used to measure TOC concentration after VLI-145 min.

The identification and measurement of benzotriazole and its intermediate degradation products were carried out using liquid chromatography–mass spectrometry (LC-MS, Thermo Quest LCQ Duo, Thermo Fisher Scientific Corporation, Waltham, MA, USA. Beta Basic-C18 HPLC column: 150×2.1 mm, ID of 5 μm , Thermo Fisher Scientific Corporation, Waltham, MA, USA.). Here, 20 μL of solution, obtained after the photocatalytic reaction, was automatically injected into the LC–MS system. The mobile phase contained 60% methanol and 40% ultrapure water, and the flow rate was 0.2 mL/min. MS conditions included an electrospray ionization interface, capillary temperature of 27 $^\circ\text{C}$ with a voltage of 19.00 V, spray voltage of 5000 V and a constant sheath gas flow rate. The spectrum was acquired in the negative ion scan mode and the m/z ranged from 50 to 600.

The incident photon flux I_0 , which was tested by a radiometer (Model FZ-A, Photoelectric Instrument Factory Beijing Normal University, China), was determined as 4.76×10^{-6} Einstein $\text{L}^{-1} \text{s}^{-1}$ under VLIR (wavelength range of 400–700 nm). The incident photon flux on the photoreactor was changed by adjusting the distance between the photoreactor and the Xe arc lamp.

The photonic efficiency was calculated in accordance with the following Equation (5):

$$\phi = R/I_0 \quad (5)$$

where ϕ was the photonic efficiency (%), R was the degradation rate of benzotriazole ($\text{mol L}^{-1} \text{s}^{-1}$), and I_0 was the incident photon flux ($\text{Einstein L}^{-1} \text{s}^{-1}$).

4. Conclusions

For the first time, an efficient photocatalyst Gd_2YSbO_7 was successfully synthesized by the solid-phase sintering method at a high temperature. Furthermore, considering the superiority of the heterojunction construction, GZHP was synthesized by a facile solvothermal method. The photophysical properties and the photocatalytic properties of Gd_2YSbO_7 and GZHP were investigated via SEM, XRD, UV-Vis DRS and XPS tests. Based on the related tests and the analysis of the results, the prepared Gd_2YSbO_7 was pure phase and crystallized in a pyrochlore structure with the space group Fd3m. The lattice parameter and the band gap of Gd_2YSbO_7 were $a = 10.653(6)$ \AA and 2.396 eV, respectively. GZHP was proved to be an effective photocatalyst for removing benzotriazole in wastewater; after VLI-145 min, the RER of benzotriazole and total organic carbon reached 99.05% and 90.18%, respectively. The RER of benzotriazole with GZH as a photocatalyst was 1.201 times or 1.266 times or 2.094 times higher than that with Gd_2YSbO_7 , ZnBiNbO_5 or NTO as a photocatalyst after VLI-145 min. Furthermore, the kinetic constant k reached 0.0110 min^{-1} . Therefore, it could be concluded that using a GZH as photocatalyst might be a potent method for treating wastewater polluted by benzotriazole. A degradation mechanism for benzotriazole was proposed, and nine intermediate products were detected during the degradation process of benzotriazole; as a result, the oxidation reaction and methylation reactions of the triazole ring were realized during the PHD process of benzotriazole. Finally, conceivable photodegradation pathways for the degradation of benzotriazole were presented.

Supplementary Materials: The following supporting information can be downloaded at: <https://www.mdpi.com/article/10.3390/catal12020159/s1>, Figure S1: X-ray powder diffraction patterns of ZnBiNbO_5 and JCPDS of $\text{Y}_2\text{Ti}_2\text{O}_7$; Figure S2: Atomic structure of ZnBiNbO_5 . (Red atom: O,

cyan atom: Zn, purple atom: Bi or Nb.); Table S1. Structural parameters of Gd_2YSbO_7 prepared by solid state reaction method. Table S2: Structural parameters of $ZnBiNbO_5$ prepared by solid state reaction method; Figure S3. (a) UV-Vis diffuse reflectance spectrum of $ZnBiNbO_5$ sample; (b) Plot of $(\alpha h\nu)^{1/2}$ versus $h\nu$ for $ZnBiNbO_5$; (c) UV-Vis diffuse reflectance spectrum of Gd_2YSbO_7 sample; (d) Plot of $(\alpha h\nu)^{1/2}$ versus $h\nu$ for Gd_2YSbO_7 sample; Figure S4. Concentration variation curves of benzotriazole during photocatalytic degradation of benzotriazole in the absence of photocatalyst under VLIR.; Table S3: The removal rate of benzotriazole with $Gd_2YSbO_7/ZnBiNbO_5$ heterojunction, S-TiO₂, N-TiO₂, C-TiO₂ or CdS-TiO₂ as photocatalyst; Figure S5: (a) Observed first-order kinetic plots for the photocatalytic degradation of benzotriazole with $Gd_2YSbO_7/ZnBiNbO_5$ heterojunction as photocatalyst or with Gd_2YSbO_7 as photocatalyst or with $ZnBiNbO_5$ as photocatalyst or with NTO as photocatalyst under VLIR; (b) Observed first-order kinetic plots for total organic carbon during photocatalytic degradation of benzotriazole in chemical industry wastewater with $Gd_2YSbO_7/ZnBiNbO_5$ heterojunction as photocatalyst or with Gd_2YSbO_7 as photocatalyst or with $ZnBiNbO_5$ as photocatalyst or with NTO as photocatalyst under VLIR.; Figure S6. Observed first-order kinetic plots for the photocatalytic degradation of benzotriazole with $Gd_2YSbO_7/ZnBiNbO_5$ heterojunction as photocatalyst under VLIR for three cycle degradation tests; Figure S7: Nyquist impedance plots of $Gd_2YSbO_7/ZnBiNbO_5$ heterojunction photocatalyst or Gd_2YSbO_7 photocatalyst or $ZnBiNbO_5$ photocatalyst; Figure S8: (a) Schematic representation of the synthesis process of the Gd_2YSbO_7 ; (b) Schematic representation of the synthesis process of the $ZnBiNbO_5$; (c) Schematic representation of the synthesis process of the $Gd_2YSbO_7/ZnBiNbO_5$ heterojunction photocatalyst.

Author Contributions: Conceptualization, Y.Y. and J.L.; methodology, Y.Y. and J.L.; software, Y.Y. and J.L.; validation, Y.Y. and J.L.; formal analysis, Y.Y. and J.L.; investigation, Y.Y. and J.L.; resources, Y.Y. and J.L.; data curation, Y.Y. and J.L.; writing—original draft preparation, Y.Y. and J.L.; writing—review and editing, Y.Y. and J.L.; visualization, Y.Y. and J.L.; supervision, Y.Y. and J.L.; project administration, Y.Y. and J.L.; funding acquisition, J.L. All authors have read and agreed to the published version of the manuscript.

Funding: This study was supported by the Scientific and Technical Innovation Leading Personnel and Team Foundation for Middle-aged and Young Scientist of Science and Technology Bureau of Jilin Province of China (Grant No. 20200301033RQ), by the Free Exploring Key Item of Natural Science Foundation of Science and Technology Bureau of Jilin Province of China (Grant No. YDZJ202101ZYTS161), by the Industrial Technology Research and Development Fund of Jilin Province Capital Development Fund on Budget in 2021 of Jilin Province Development and Reform Commission of China (Grant No. 2021C037-1), by the Project Funded for Innovational and Enterprising Talents of Department of Human Resource and Social Security of Jilin Province of China (Grant No. 2020033), by the Scientific Research Planning Project of the Education Department of Jilin Province of China (Grant No. JJKH20200832KJ), by the Scientific Research Planning Project of the Education Department of Jilin Province of China (Grant No. JJKH20210885KJ), by Natural Science Foundation of Changchun Normal University (Grant No. [2019]13), by the Scientific Research Initiating Foundation for Advanced Doctor of Changchun Normal University.

Acknowledgments: Thanks to Dongxu Yu for his contribution to the XPS data analysis. Thanks to Zhijie Wei, Bowen Niu, Bingbing Ma and Wenlu Liu for their contribution to the data analysis and making a drawing.

Conflicts of Interest: The authors declare no conflict of interest.

References

1. Huntscha, S.; Hofstetter, T.B.; Schymanski, E.L.; Spahr, S.; Hollender, J. Biotransformation of benzotriazoles: Insights from transformation product identification and compound-specific isotope analysis. *Environ. Sci. Technol.* **2014**, *48*, 4435–4443. [[CrossRef](#)] [[PubMed](#)]
2. Luan, J.; Huang, P.Q. Photophysical and photocatalytic properties of $BiSnSbO_6$ under visible light irradiation. *Materials* **2018**, *11*, 491. [[CrossRef](#)] [[PubMed](#)]
3. Voutsas, D.; Hartmann, P.; Schaffner, C.; Giger, W. Benzotriazoles, alkylphenols and bisphenol A in municipal wastewaters and in the Glatt River, Switzerland. *Environ. Sci. Pollut. Res.* **2006**, *13*, 333–341. [[CrossRef](#)] [[PubMed](#)]
4. Liu, R.; Ruan, T.; Wang, T.; Song, S.; Guo, F.; Jiang, G. Determination of nine benzotriazole UV stabilizers in environmental water samples by automated on-line solid phase extraction coupled with high-performance liquid chromatography—tandem mass spectrometry. *Talanta* **2014**, *120*, 158–166. [[CrossRef](#)]

5. Lai, H.; Ying, G.; Ma, Y.; Chen, Z.; Chen, F.; Liu, Y. Occurrence and dissipation of benzotriazoles and benzotriazole ultraviolet stabilizers in biosolid-amended soils. *Environ. Toxicol. Chem.* **2014**, *33*, 761–767. [[CrossRef](#)]
6. Jia, Y.; Bakken, L.R.; Breedveld, G.D.; Aagaard, P.; Frostegård, Å. Organic compounds that reach subsoil may threaten groundwater quality: Effect of benzotriazole on degradation kinetics and microbial community composition. *Soil Biol. Biochem.* **2006**, *38*, 2543–2556. [[CrossRef](#)]
7. Nakata, H.; Murata, S.; Filatreau, J. Occurrence and concentrations of benzotriazole UV stabilizers in marine organisms and sediments from the Ariake Sea, Japan. *Environ. Sci. Technol.* **2009**, *43*, 6920–6926. [[CrossRef](#)]
8. Kim, J.; Ramaswamy, B.R.; Chang, K.; Isobe, T.; Tanabe, S. Multiresidue analytical method for the determination of antimicrobials, preservatives, benzotriazole UV stabilizers, flame retardants and plasticizers in fish using ultra high performance liquid chromatography coupled with tandem mass spectrometry. *J. Chromatogr. A* **2011**, *1218*, 3511–3520. [[CrossRef](#)]
9. Hem, L.J.; Hartnik, T.; Roseth, R.; Breedveld, G.D. Photochemical degradation of benzotriazole. *J. Environ. Sci. Health A* **2003**, *38*, 471–481. [[CrossRef](#)]
10. Hollingsworth, J.; Sierra-Alvarez, R.; Zhou, M.; Ogden, K.L.; Field, J.A. Anaerobic biodegradability and methanogenic toxicity of key constituents in copper chemical mechanical planarization effluents of the semiconductor industry. *Chemosphere* **2005**, *59*, 1219–1228. [[CrossRef](#)]
11. Xu, J.; Li, L.; Guo, C.S.; Zhang, Y.; Wang, S.F. Removal of benzotriazole from solution by BiOBr photocatalysis under simulated solar irradiation. *Chem. Eng. J.* **2013**, *221*, 230–237. [[CrossRef](#)]
12. Zhe, L.; Shirley, A.S.; Thomas, E.P.; Amila, O.D.S. Occurrence and fate of substituted diphenylamine antioxidants and benzotriazole UV stabilizers in various Canadian wastewater treatment processes. *Water Res.* **2017**, *124*, 158–166.
13. Zhe, L.; Amila, O.D.S.; Thomas, E.P.; Cyril, J.C.; Gerald, R.T.; Mark, R.S.; Derek, C.G.M. Distribution, partitioning and bioaccumulation of substituted diphenylamine antioxidants and benzotriazole UV stabilizers in an Urban Creek in Canada. *Environ. Sci. Technol.* **2016**, *50*, 9089–9097.
14. Javaid, R.; Qazi, U.Y. Catalytic oxidation process for the degradation of synthetic dyes: An overview. *Inter. J. Env. Res. Pub. Heal.* **2019**, *16*, 2066. [[CrossRef](#)] [[PubMed](#)]
15. Aarathi, T.; Narahari, P.; Madras, G. Photocatalytic degradation of azure and sudan dyes using nano TiO₂. *J. Hazard. Mater.* **2007**, *149*, 725–734. [[CrossRef](#)]
16. Rahman, M.U.; Qazi, U.Y.; Hussain, T.; Nadeem, N.; Zahid, M.; Bhatti, H.N.; Shahid, I. Solar driven photocatalytic degradation potential of novel graphitic carbon nitride based nano zero-valent iron doped bismuth ferrite ternary composite. *Opt. Mater.* **2021**, *120*, 111408. [[CrossRef](#)]
17. Tahmasebi, N.; Esmaeilpour, H.; Movahedifard, F.; Hakimifard, A.; Moayeri, H. Fabrication of a novel MoO₃/Cs₃PMo₁₂O₄₀ composite for photocatalytic decolorization of rhodamine B. *Mat. Sci. Semicon. Proc.* **2021**, *131*, 105876. [[CrossRef](#)]
18. Mokhtari, F.; Tahmasebi, N. Hydrothermal synthesis of W-doped BiOCl nanoplates for photocatalytic degradation of rhodamine B under visible light. *J. Phys. Chem. Solids* **2021**, *149*, 109804. [[CrossRef](#)]
19. Subhan, M.A.; Rifat, T.P.; Saha, P.C.; Alam, M.M.; Asiri, A.M.; Rahman, M.M.; Akter, S.; Raihan, T.; Azad, A.K.; Uddin, J. Enhanced visible light-mediated photocatalysis, antibacterial functions and fabrication of a 3-chlorophenol sensor based on ternary Ag₂O-SrO-CaO. *RSC Adv.* **2020**, *10*, 11274–11291. [[CrossRef](#)]
20. Rizzo, L.; Della Sala, A.; Fiorentino, A.; Li Puma, G. Disinfection of urban wastewater by solar driven and UV lamp—TiO₂ photocatalysis: Effect on a multi drug resistant Escherichia coli strain. *Water Res.* **2014**, *53*, 145–152. [[CrossRef](#)]
21. Sakai, T.; Da Loves, A.; Okada, T.; Mishima, S. Titania/CnTAB nanoskeleton as adsorbent and photocatalyst for removal of alkylphenols dissolved in water. *J. Hazard. Mater.* **2013**, *248*, 487–495. [[CrossRef](#)] [[PubMed](#)]
22. Kapoor, P.N.; Uma, S.; Rodriguez, S.; Klabunde, K.J. Aerogel processing of MTi₂O₅ (M = Mg, Mn, Fe, Co, Zn, Sn) compositions using single source precursors: Synthesis, characterization and photocatalytic behavior. *J. Mol. Catal. A Chem.* **2005**, *229*, 145–150. [[CrossRef](#)]
23. Zhang, H.S.; Wen, Z.Y.; Zhao, Y.D.; Li, G.; Li, Z.J. Preparation, characterization of A₂Ce₂O₇ (A = La and Gd) and their photocatalytic properties. *Energy Environ. Focus.* **2015**, *4*, 324–329.
24. Ladan, R.; Alireza, H.; Mohammad, S. High efficient solar light photocatalytic degradation of malachite green by solid state synthesized Bi₂Sn₂O₇ and Bi₂M_xSn₂O₇ (M = Y³⁺, Eu³⁺, Gd³⁺ and Yb³⁺) nanomaterials. *J. Nanoanal.* **2020**, *7*, 1–17.
25. Hebeish, A.A.; Abdelhady, M.M.; Youssef, A.M. TiO₂ nanowire and TiO₂ nanowire doped Ag-PVP nanocomposite for antimicrobial and self-cleaning cotton textile. *Carbohydr. Polym.* **2013**, *91*, 549–559. [[CrossRef](#)] [[PubMed](#)]
26. Chen, J.; Wu, X.J.; Yin, L.; Li, B.; Hong, X.; Fan, Z.; Chen, B.; Xue, C.; Zhang, H. One-pot synthesis of CdS nanocrystals hybridized with single-layer transition-metal dichalcogenide nanosheets for efficient photocatalytic hydrogen evolution. *Angew. Chem. Int. Ed. Engl.* **2015**, *54*, 1210–1214.
27. Zhang, Z.; Li, A.; Cao, S.W.; Bosman, M.; Li, S.; Xue, C. Direct evidence of plasmon enhancement on photocatalytic hydrogen generation over Au/Pt-decorated TiO₂ nanofibers. *Nanoscale* **2014**, *6*, 5217–5222. [[CrossRef](#)]
28. Zhang, N.; Shi, J.; Mao, S.S.; Guo, L. Co₃O₄ quantum dots: Reverse micelle synthesis and visible-light-driven photocatalytic overall water splitting. *Chem. Commun.* **2014**, *50*, 2002–2004. [[CrossRef](#)]
29. Wang, X.; Xu, Q.; Li, M.; Shen, S.; Wang, Y.; Feng, Z.; Shi, J.; Han, H.; Li, C. Photocatalytic overall water splitting promoted by an alpha-beta phase junction on Ga₂O₃. *Angew. Chem. Int.* **2012**, *51*, 13089–13092. [[CrossRef](#)]

30. Huang, J.G.; Zhao, X.G.; Zheng, M.Y.; Li, S.; Wang, Y.; Liu, X.J. Preparation of N-doped TiO₂ by oxidizing TiN and its application on phenol degradation. *Water Sci. Technol.* **2013**, *68*, 934–939. [[CrossRef](#)]
31. Mohammadi, K.; Sadeghi, M.; Azimirad, R. Facile synthesis of SrFe₁₂O₁₉ nanoparticles and its photocatalyst application. *J. Mater. Sci. Mater. EL* **2017**, *28*, 10042–10047. [[CrossRef](#)]
32. Mohammadi, K.; Sadeghi, M.; Azimirad, R.; Ebrahimi, M. Barium hexaferrite nanoparticles: Morphology-controlled preparation, characterization and investigation of magnetic and photocatalytic properties. *J. Mater. Sci. Mater. EL* **2017**, *28*, 9983–9988. [[CrossRef](#)]
33. Shieh, D.L.; Lin, Y.S.; Yeh, J.H.; Chen, S.C.; Lin, B.C.; Lin, J.L. N-doped, porous TiO₂ with rutile phase and visible light sensitive photocatalytic activity. *Chem. Commun.* **2012**, *48*, 2528–2530. [[CrossRef](#)] [[PubMed](#)]
34. Zhou, X.; Lu, J.; Jiang, J.; Li, X.; Lu, M.; Yuan, G.; Wang, Z.; Zheng, M.; Seo, H.J. Simple fabrication of N-doped mesoporous TiO₂ nanorods with the enhanced visible light photocatalytic activity. *Nanoscale Res. Lett.* **2014**, *9*, 34. [[CrossRef](#)]
35. Chen, X.; Burda, C. The electronic origin of the visible-light absorption properties of C-, N- and S-doped TiO₂ nanomaterials. *J. Am. Chem. Soc.* **2008**, *130*, 5018–5019. [[CrossRef](#)]
36. Li, H.; Zhang, X.; Huo, Y.; Zhu, J. Supercritical preparation of a highly active S-doped TiO₂ photocatalyst for methylene blue mineralization. *Environ. Sci. Technol.* **2007**, *41*, 4410–4414. [[CrossRef](#)]
37. Li, Z.; Ding, D.; Ning, C. P-Type hydrogen sensing with Al- and V-doped TiO₂ nanostructures. *Nanoscale Res. Lett.* **2013**, *8*, 25. [[CrossRef](#)]
38. Pan, L.; Wang, S.; Zou, J.J.; Huang, Z.F.; Wang, L.; Zhang, X. Ti³⁺-defected and V-doped TiO₂ quantum dots loaded on MCM-41. *Chem. Commun.* **2014**, *50*, 988–990. [[CrossRef](#)]
39. Zhang, Z.; Shao, C.; Zhang, L.; Li, X.; Liu, Y. Electrospun nanofibers of V-doped TiO₂ with high photocatalytic activity. *J. Colloid. Interf. Sci.* **2010**, *351*, 57–62. [[CrossRef](#)]
40. Liu, G.; Han, C.; Pelaez, M.; Zhu, D.; Liao, S.; Likodimos, V.; Ioannidis, N.; Kontos, A.G.; Falaras, P.; Dunlop, P.S.; et al. Synthesis, characterization and photocatalytic evaluation of visible light activated C-doped TiO₂ nanoparticles. *Nanotechnology* **2012**, *23*, 294003. [[CrossRef](#)]
41. Yu, J.; Zhou, P.; Li, Q. New insight into the enhanced visible-light photocatalytic activities of B-, C- and B/C-doped anatase TiO₂ by first-principles. *Phys. Chem. Chem. Phys.* **2013**, *15*, 12040–12047. [[CrossRef](#)]
42. Zhang, W.J.; Ma, Z.; Du, L.; Li, H. Role of PEG4000 in sol-gel synthesis of Sm₂Ti₂O₇ photocatalyst for enhanced activity. *J. Alloy. Compd.* **2017**, *704*, 26–31. [[CrossRef](#)]
43. Wang, S.X.; Li, W.; Wang, S.; Jiang, J.M.; Chen, Z.H. Synthesis of well-defined hierarchical porous La₂Zr₂O₇ monoliths via non-alkoxidesol-gel process accompanied by phase separation. *Micropor. Mesopor. Mat.* **2016**, *221*, 32–39. [[CrossRef](#)]
44. Zou, Z.; Ye, J.; Arakawa, H. Preparation, structural and photophysical properties of Bi₂InNbO₇ compound. *J. Mater. Sci.* **2000**, *19*, 1909–1911.
45. Shin, H.; Byun, T.H. Effect of Pt loading onto ball-milled TiO₂ on the visible-light photocatalytic activity to decompose rhodamine B. *Res. J. Chem. Environ.* **2013**, *17*, 41–46.
46. Kanhere, P.; Shenai, P.; Chakraborty, S.; Ahuja, R.; Zheng, J.; Chen, Z. Mono- and co-doped NaTaO₃ for visible light photocatalysis. *Phys. Chem. Chem. Phys.* **2014**, *16*, 16085–16094. [[CrossRef](#)]
47. Daskalaki, V.M.; Antoniadou, M.; Li Puma, G.; Kondarides, D.I.; Lianos, P. Solar light-responsive Pt/CdS/TiO₂ photocatalysts for hydrogen production and simultaneous degradation of inorganic or organic sacrificial agents in wastewater. *Environ. Sci. Technol.* **2010**, *44*, 7200–7205. [[CrossRef](#)]
48. Luan, J.F.; Zhao, W.; Feng, J.W.; Cai, H.L.; Zheng, Z.; Pan, B.C.; Wu, X.S.; Zou, Z.G.; Li, Y.M. Structural, photophysical and photocatalytic properties of novel Bi₂AlVO₇. *J. Hazard. Mater.* **2009**, *164*, 781–789. [[CrossRef](#)]
49. Xing, C.C.; Zhang, Y.; Liu, Y.P.; Wang, X.; Li, J.S.; Martinez-Alanis, P.R.; Spadaro, M.C.; Guardia, P.; Arbiol, J.; Llorca, J.; et al. Photodehydrogenation of ethanol over Cu₂O/TiO₂ heterostructures. *Nanomaterials* **2021**, *11*, 1399. [[CrossRef](#)]
50. Stathi, P.; Solakidou, M.; Deligiannakis, Y. Lattice defects engineering in W-, Zr-doped BiVO₄ by flame spray pyrolysis: Enhancing photocatalytic O₂ evolution. *Nanomaterials* **2021**, *11*, 501. [[CrossRef](#)]
51. Thomas, A.M.; Peter, J.; Nagappan, S.; Mohan, A.; Ha, C.S. Dual stimuli-responsive copper nanoparticles decorated SBA-15: A highly efficient catalyst for the oxidation of alcohols in water. *Nanomaterials* **2020**, *10*, 2051. [[CrossRef](#)]
52. Zou, Y.; Shi, J.W.; Ma, D.; Fan, Z.; Lu, L.; Niu, C. In situ synthesis of C-doped TiO₂@g-C₃N₄ core-shell hollow nanospheres with enhanced visible-light photocatalytic activity for H₂ evolution. *Chem. Eng. J.* **2017**, *322*, 435–444. [[CrossRef](#)]
53. Yu, Y.; Cao, C.Y.; Liu, H.; Li, P.; Wei, F.F.; Jiang, Y.; Song, W.G. A Bi/BiOCl heterojunction photocatalyst with enhanced electron-hole separation and excellent visible light photodegrading activity. *J. Mater. Chem. A* **2014**, *2*, 1677–1681. [[CrossRef](#)]
54. Wang, P.Q.; Bai, Y.; Luo, P.Y.; Liu, J.Y. Ag₂O/Ag₃PO₄ heterostructures: Highly efficient and stable visible-light-induced photocatalyst for degradation of methyl orange and phenol. *Micro Nano Lett.* **2013**, *8*, 340–344. [[CrossRef](#)]
55. Tang, Y.; Tao, Y.; Zhou, T.; Yang, B.; Wang, Q.; Zhu, Z.; Xie, A.; Luo, S.; Yao, C.; Li, X. Direct Z-scheme La_{1-x}Ce_xMnO₃ catalyst for photothermal degradation of toluene. *Environ. Sci. Pollut. R* **2019**, *26*, 36832–36844. [[CrossRef](#)]
56. Wang, J.H.; Zou, Z.G.; Ye, J.H. Synthesis, structure and photocatalytic property of a new hydrogen evolving photocatalyst Bi₂InTaO₇. *Mater. Sci. Forum.* **2003**, *423*, 485–490. [[CrossRef](#)]
57. Kohno, M.; Ogura, S.; Sato, K.; Inoue, Y. Properties of photocatalysts with tunnel structures: Formation of a surface lattice O-radical by the UV irradiation of BaTi₄O₉ with a pentagonal-prism tunnel structure. *Chem. Phys. Lett.* **1997**, *267*, 72–76. [[CrossRef](#)]

58. Kudo, A.; Kato, H.; Nakagawa, S. Water splitting into H₂ and O₂ on new Sr₂M₂O₇ (M = Nb and Ta) photocatalysts with layered perovskite structures: Factors affecting the photocatalytic activity. *J. Phys. Chem. B* **2000**, *104*, 571–575. [[CrossRef](#)]
59. Nowak, M.; Kauch, B.; Szperlich, P. Determination of energy band gap of nanocrystalline SbSI. *Rev. Sci. Instrum.* **2009**, *80*, 046107. [[CrossRef](#)]
60. Zhou, F.; Kang, K.; Maxisch, T.; Ceder, G.; Morgan, D. The electronic structure and band gap of LiFePO₄ and LiMnPO₄. *Solid State Commun.* **2004**, *132*, 181–186. [[CrossRef](#)]
61. Tauc, J.; Grigorov, R.; Vancu, A. Optical properties and electronic structure of amorphous germanium. *Phys. Status Solidi.* **1966**, *15*, 627–637. [[CrossRef](#)]
62. Butler, M.A. Photoelectrolysis with YFeO₃ electrodes. *J. Appl. Phys.* **1977**, *48*, 1914–1920. [[CrossRef](#)]
63. Cui, B.Y.; Cui, H.T.; Li, Z.R.; Dong, H.Y.; Li, X.; Zhao, L.F.; Wang, J.W. Novel Bi₃O₅I₂ hollow microsphere and its enhanced photocatalytic activity. *Catalysts* **2019**, *9*, 709. [[CrossRef](#)]
64. Vallejo, W.; Cantillo, A.; Salazar, B.; Diaz-Urbe, C.; Ramos, W.; Romero, E.; Hurtado, M. Comparative study of ZnO thin films doped with transition metals (Cu and Co) for methylene blue photodegradation under visible irradiation. *Catalysts*. **2020**, *10*, 528. [[CrossRef](#)]
65. Qazi, U.Y.; Javaid, R.; Zahid, M.; Tahir, N.; Afzal, A.; Lin, X.M. Bimetallic NiCo-NiCoO₂ nano-heterostructures embedded on copper foam as a self-supported bifunctional electrode for water oxidation and hydrogen production in alkaline media. *Int. J. Hydrogen Energ.* **2021**, *46*, 18936–18948. [[CrossRef](#)]
66. Qazi, U.Y.; Javaid, R.; Tahir, N.; Jamil, A.; Afzal, A. Design of advanced self-supported electrode by surface modification of copper foam with transition metals for efficient hydrogen evolution reaction. *Int. J. Hydrogen Energ.* **2020**, *45*, 33396–33406. [[CrossRef](#)]
67. Deonikar, V.G.; Patil, S.S.; Tamboli, M.S.; Ambekar, J.D.; Kulkarni, M.V.; Panmand, R.P.; Umarji, G.G.; Shinde, M.D.; Rane, S.B.; Munirathnam, N.R.; et al. Growth study of hierarchical Ag₃PO₄/LaCO₃OH heterostructures. *Phys. Chem. Chem. Phys.* **2017**, *19*, 20541–20550. [[CrossRef](#)]
68. Patil, S.S.; Tamboli, M.S.; Deonikar, V.G.; Umarji, G.G.; Ambekar, J.D.; Kulkarni, M.V.; Kolekar, S.S.; Kale, B.B.; Patil, D.R. Magnetically separable Ag₃PO₄/NiFe₂O₄ composites with enhanced photocatalytic activity. *Dalton Trans.* **2015**, *44*, 20426–20434. [[CrossRef](#)]
69. Jiang, L.B.; Yuan, X.Z.; Zeng, G.M.; Liang, J.; Chen, X.H.; Yu, H.B.; Wang, H.; Wu, Z.B.; Zhang, J.; Xiong, T. In-situ synthesis of direct solid-state dual Z-scheme WO₃/g-C₃N₄/Bi₂O₃ photocatalyst for the degradation of refractory pollutant. *Appl. Catal. B* **2018**, *227*, 376–385. [[CrossRef](#)]
70. Cao, W.; Jiang, C.Y.; Chen, C.; Zhou, H.F.; Wang, Y.P. A novel Z-scheme CdS/Bi₄O₅Br₂ heterostructure with mechanism analysis: Enhanced photocatalytic performance. *J. Alloys Compd.* **2021**, *861*, 158554. [[CrossRef](#)]
71. Zhuang, Y.; Zhou, M.; Gu, J.; Li, X. Spectrophotometric and high performance liquid chromatographic methods for sensitive determination of bisphenol A. *Spectrochim. Acta A* **2013**, *122*, 153–157. [[CrossRef](#)] [[PubMed](#)]